A computational investigation of the instability of the detached shear layers in the wake of a circular cylinder

MAN MOHAN RAI†

NASA Ames Research Center, Moffett Field, CA 94035, USA

Cylinder wakes have been studied extensively over several decades to better understand the basic flow phenomena encountered in such flows. The physics of the very near wake of the cylinder is perhaps the most challenging of them all. This region comprises the two detached shear layers, the recirculation region and wake flow. A study of the instability of the detached shear layers is important because these shear layers have a considerable impact on the dynamics of the very near wake. It has been observed experimentally that during certain periods of time that are randomly distributed, the measured fluctuating velocity component near the shear layers shows considerable amplification and it subsequently returns to its normal level (intermittency). Here, direct numerical simulations are used to accomplish a number of objectives such as confirming the presence of intermittency (computationally) and shedding light on processes that contribute significantly to intermittency and shear-layer transition/breakdown. Velocity time traces together with corresponding instantaneous vorticity contours are used in deciphering the fundamental processes underlying intermittency and shear-layer transition. The computed velocity spectra at three locations along the shear layer are provided. The computed shear-layer frequency agrees well with a power-law fit to experimental data.

Key words: instability, mathematical foundations, wakes/jets

---

1. Introduction

The interest in turbulent wakes spans the spectrum from an intellectual pursuit to understand the complex underlying physics to a critical need in aeronautical engineering and other disciplines to predict component/system performance and reliability. Cylinder wakes have been studied extensively over several decades to gain a better understanding of the basic flow phenomena that are encountered in such flows. Experimental, computational and theoretical means have been employed in this effort. While much has been accomplished there are many important issues that need to be resolved. The physics of the very near wake of the cylinder (less than three diameters downstream) is perhaps the most challenging of them all. This region comprises the two detached shear layers, the recirculation region and wake flow. The interaction amongst these three components is to some extent still a matter of conjecture. Experimental techniques have generated a large percentage of the data

† Email address for correspondence: man.m.rai@nasa.gov

that have provided us with the current state of understanding of the subject. More recently, computational techniques have been used to simulate cylinder wakes, and the data from such simulations are being used to both refine our understanding of such flows and provide new insights. A review of the large body of experimental and some recent computational investigations of cylinder wakes is provided in Williamson (1996).

A study of the instability of the detached shear layers is important because these shear layers have a considerable impact on the dynamics of the very near wake. Early researchers in the field discovered that in a certain Reynolds number range, transition to turbulence occurs within the detached shear layers and that the large-scale vortices in the near wake are turbulent (Roshko 1953). It was also observed that the transition process moved upstream within the shear layer with increasing Reynolds number. A fundamental discovery by Bloor (1964), using measurements of the fluctuating longitudinal velocity, was the presence of what were called 'transition waves' in the detached shear layers. These transition waves are of a higher frequency than the shedding, or Strouhal frequency (ω_{st}) and are responsible for a broadband peak in velocity spectra obtained near the shear layers. The ratio of the shear-layer frequency (ω_{SL}, the frequency at which the peak occurs) to the Strouhal frequency was determined to be a function of the Reynolds number. A first theory that this ratio was proportional to the square root of the Reynolds number was proposed in Bloor (1964). Since then the theory has been refined and the exponent has been more accurately determined to be around 0.67. Numerous sets of experimental data from different experiments also confirm the larger value for the exponent (Prasad & Williamson 1997).

An experimental study of the three-dimensional structure of the shear-layer vortices is presented by Wei & Smith (1986). A number of observations as well as hypotheses are made therein. The data were found to indicate that the shear-layer vortices exhibit a cellular structure. These cells are aligned with other similar cells in the streamwise direction, with newer ones positioned behind older ones. The authors also offer a theory for the deformation of the largely spanwise vortices that they observed in the upstream portion of the shear layer. Early deformation is ascribed to the susceptibility of these vortices to three-dimensional instabilities that results in their stretching in the streamwise direction. This results in the spanwise vortices assuming a spanwise wavy structure with peaks appearing downstream and valleys upstream within the shear layer. This in turn results in streamwise vorticity (segments of the vortex that are largely aligned with the *x*-axis) which then undergoes rapid deformation because the Kármán vortex associated with the shear layer in question makes the peaks of the spanwise wavy structure move faster than the valleys. Thus, the Kármán vortices provide the necessary streamwise vortex stretching for the evolution of shear-layer vortices. They also theorize that the counter-rotating Kármán vortex associated with the adjacent shear layer tends to push the valleys of the shear-layer vortex upstream, thus enhancing the stretching process and resulting in a rapid evolution of the shear-layer vortices.

Several fundamental aspects of the instability of the detached shear layer are explored by Unal & Rockwell (1988). Cylinder wake data from experiments conducted in a water channel are used to demonstrate the exponential growth of the amplitude of the fluctuating component of the velocity (both maximum value within the shear layer and the value at the edge of the shear layer) with streamwise distance. Velocity spectra across the shear layer show two dominant frequencies: one is the shedding frequency and the other the shear-layer frequency. The former was found to dominate

in the lower part of the shear layer (closer to the centreline) and the latter in the upper part. Peaks in the spectra were also observed at two and three times the shedding frequency and at $(\omega_{SL} \pm \omega_{st})$. The authors ascribe the latter set of peaks to nonlinear interactions between fluctuations at shedding frequency and those at the shear-layer frequency. They also found that there was no evidence of coalescence of successive shear-layer vortices that should be observable as subharmonics of the shear-layer frequency.

One aspect of cylinder wakes that has received attention in the recent past is the manifestation of intermittency in velocity signals in the proximity of the detached shear layer. It has been observed experimentally that during certain periods of time that are randomly distributed, the measured fluctuating velocity component shows considerable amplification and subsequently returns to its normal level. The mechanism behind this amplification is not fully understood. This intermittency is thought to be because of the random movement of the transition point in the upstream direction within the detached layer, which in turn is influenced by temporal changes in near-wake three-dimensional structures (Prasad & Williamson 1997). Regardless of the origin of intermittency, the role it plays in determining the dynamics of the very near wake is an important one (such as early transition). Prasad & Williamson (1997) hypothesize other aspects of intermittency as well. These hypotheses will be reviewed in detail later.

One of the important assertions of Wei & Smith (1986) is that a stationary hot-wire probe in the vicinity of the shear layer will only sense instabilities when the shear layer is close to the probe. Thus, because of the oscillation of the shear layer in the cross-stream direction, the signal obtained indicates shear-layer vortices in an intermittent fashion. The implication of this assertion is that intermittency is not a real, independent phenomenon but is observed because of the cross-stream motion of the shear layer. This point is refuted by Prasad & Williamson (1997). They argue that intermittency is observed at streamwise locations that are as far upstream as 0.6 diameters from the axis of the cylinder where cross-stream movements of the shear layer are very small. Additionally, they estimated that the cross-stream motion at 1 diameter downstream of the axis is only about 8 % of the thickness of the shear layer and thus even at this location intermittency is a real phenomenon. On the basis of cylinder wake data where the formation of Kármán vortices is suppressed, Prasad & Williamson (1997) observe that Kármán shedding alone cannot explain intermittency.

Kim & Choi (2001) present a computational investigation of the instability of the shear layer. Data from large-eddy simulations (LES) of cylinder flow at Reynolds numbers of 1600 and 3900 are interrogated to better understand the shear-layer instability. Time traces of the streamwise velocity and contours of the fluctuating component of the streamwise velocity in a plane corresponding to the spanwise direction and time (t–z plane) in the vicinity of the shear layer and three-dimensional vortex structure in the shear layer and wake are presented. The authors propose the presence of two distinct types of shear-layer instability: type A which is three-dimensional and is generated locally by a strong streamwise vortex pair underneath the shear layer, and type B which is quasi-two-dimensional and is related to Kármán vortex shedding. It is claimed that the type B instability is initiated from the disorder of the Kármán vortex shedding process and appears in phase in both the upper and lower detached shear layers. It is also conjectured that the type B instability is more likely to occur at Reynolds numbers higher than computed by the authors.

Here, direct numerical simulations (DNS) are used to confirm the presence of intermittency (computationally) and identify the fundamental processes that contribute significantly to intermittency. We rely on velocity time traces and corresponding instantaneous vorticity contours in establishing the sequence of events leading to intermittency and shear-layer transition. The computed velocity spectra at various locations along the shear layer are also provided. The computed shear-layer frequency is found to agree well with the power-law fit to experimental data provided in Prasad & Williamson (1997). The dual instability mode conjecture presented in Kim & Choi (2001) and other observations and hypotheses of Prasad & Williamson (1997) and Wei & Smith (1986) are explored here with the aid of the computed data.

2. Numerical method and computational grid

A high-order accurate upwind-biased method is utilized by Rai (2008) to investigate the claim that high-order upwind methods may be too dissipative on the generally coarser grids that are used both for LES and coarse-grid DNS. The method used in this study is an extension of the method of Rai & Moin (1993) to curvilinear grids. Sixth- and seventh-order upwind-biased finite differences are used for the convective terms in Rai (2008). Cylinder wake flow ($Re_D = 3900$) is computed without a subgrid-scale model and with nearly the same number of grid points as in the computations of Kravchenko & Moin (2000). Computed turbulence intensity profiles in the cross-stream direction and centreline velocity spectra are compared with the experimental data of Ong, Wallace & Moin (1995). The computed results agree well with experimental data and are not negatively impacted by the dissipation of the scheme. The agreement obtained is of the same quality as that obtained in Kravchenko & Moin (2000). While the computation in Kravchenko & Moin (2000) is confined to the region $x/D \leqslant 10.0$, Rai (2008) provides a second computation that extends up to $x/D \leqslant 40.0$ ($Re_D = 5830$). The computed intensity profiles are compared with the experimental data of Matsumura & Antonia (1993) and are found to be in agreement even at $x/D = 40.0$.

The cylinder computations at $Re_D = 3900$ of Rai (2008) were performed on both a baseline grid and a fine grid. The fine grid contained approximately twice as many grid points as the baseline grid. Turbulence statistics and velocity spectra obtained in the wake on these two grids were compared. Only minor differences were noted between the two sets of results, thus essentially establishing grid independence of the computed data. The data obtained on the fine grid are utilized here to explore near-wake phenomena. This multiple-zone grid is described below.

The computational region is divided into two zones to facilitate grid generation and provide adequate grid resolution for the wake. Figure 1 shows the cylinder cross-section and the two zones that together comprise the computational region. The three-dimensional zones and grids are obtained by uniformly spacing copies of their two-dimensional counterparts in the spanwise direction (z). The cylindrical zone is bounded by four boundaries: a portion of the cylinder surface, a circular external boundary and two zonal boundaries (top and bottom) that interface with the wake zone. It captures the flow field upstream of the cylinder and the boundary layer on the front of the cylinder. The wake zone is constructed to provide optimum grid resolution for the detached shear layers and the wake of the cylinder. The boundaries of this zone are comprised of the back of the cylinder, the upper and lower boundaries and the exit boundary. Both the upper and lower boundaries consist of a zonal boundary
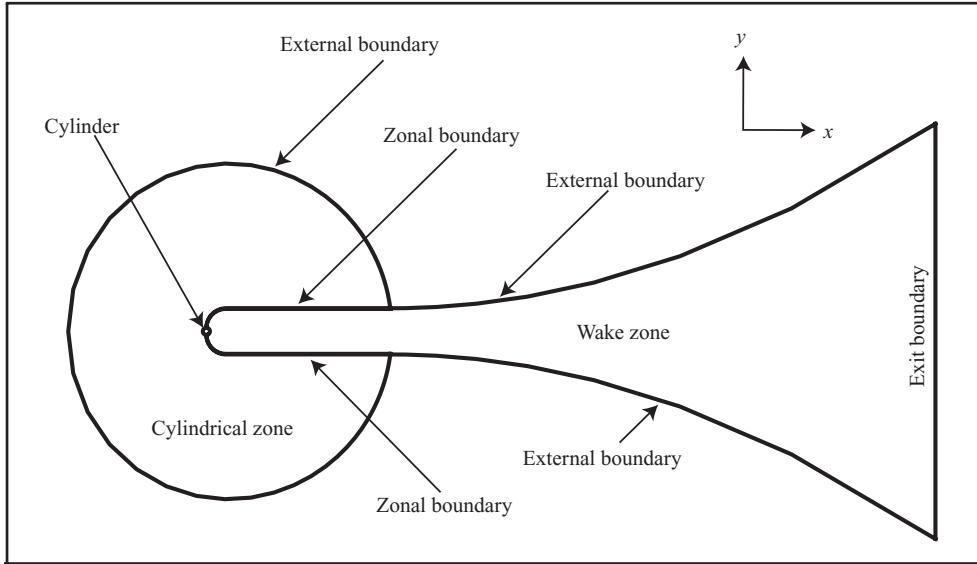
FIGURE 1. Mid-span cylinder section and multiple zone discretization of the computational region.

segment that interfaces with the cylindrical zone and a second segment that serves as an external boundary.

The diameter of the circular external boundary of the cylindrical zone is $25D$, where D is the diameter of the cylinder. The exit boundary of the wake zone is at $x/D = 103.0$ (the centre of the cylinder is at $x/D = 0.0$), and the vertical extent of this boundary is $58.5D$. In the vicinity of the cylinder, where the upper and lower boundaries of the wake zone are horizontal, the vertical extent of this zone is $6.5D$ and is large enough to completely contain the computed turbulent wake. The spanwise dimension of the computational region is πD (as in Kravchenko & Moin 2000). The streamwise extent of the well-resolved region of the wake zone extends to $x/D = 14.0$ although the region of interest in this computation was only up to $x/D = 10.0$. The fine grid continues further than required to minimize any effect of grid coarsening, which begins at $x/D = 14.0$, on the computed wake in the first 10 diameters.

Figure 2 shows representative grids in the vicinity of the cylinder in both zones. These grids were generated with an algebraic grid generator. Both the grids have the same spacing in the wall-normal direction at the cylinder surface, $\Delta n = 0.0032D$. The grid in the wake zone quickly transitions from curvilinear near the cylinder to rectangular downstream. The wake grid was constructed with 351 grid points in the streamwise direction, 121 in the cross-stream direction and 60 in the spanwise direction ($351 \times 121 \times 60$). At $x/D = 10.0$, the resolutions achieved along the centreline in these directions are $\Delta x/\eta = 4.05$, $\Delta y/\eta = 3.81$ and $\Delta z/\eta = 5.18$, respectively. Here η is the estimated Kolmogorov length scale at $x/D = 10.0$. The spacing in the y-direction, Δy, increases slightly from the centreline to the upper and lower boundaries of the wake grid. Beyond $x/D = 14.0$, the grid coarsens gradually in the streamwise direction. In addition to reducing the computational costs incurred, this coarsening dissipates the wake to a degree that inviscid exit boundary conditions can be employed at the exit boundary of the wake zone. The cylindrical grid was constructed with 81 points in the wall-tangential direction, 81 points in the wall-normal direction and 60 points in
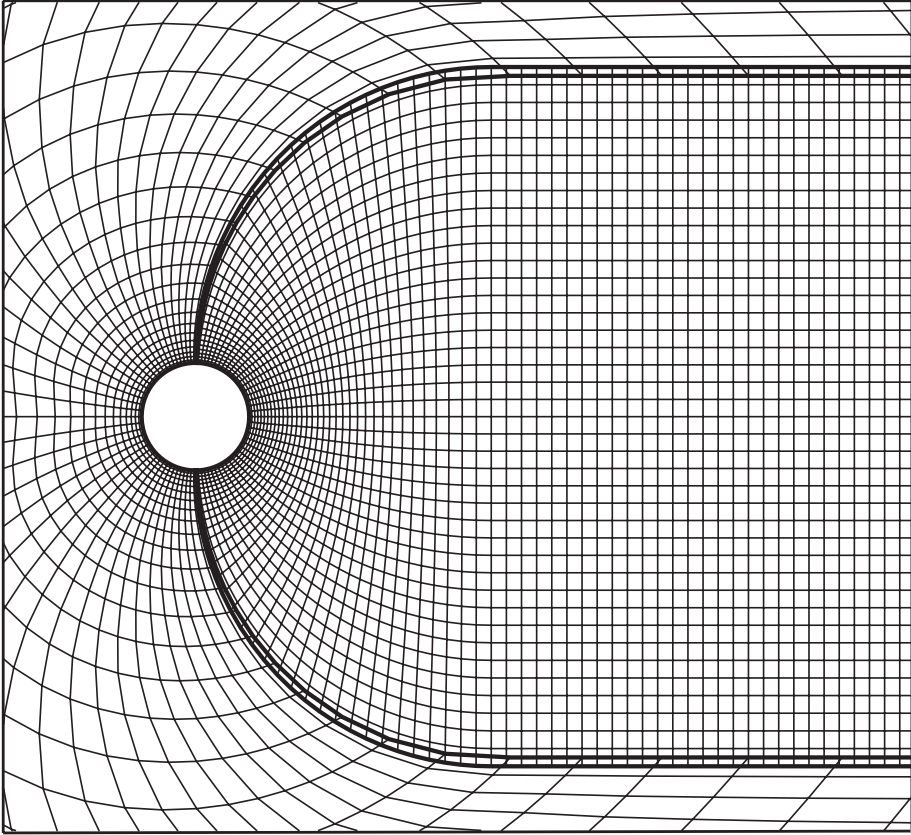
FIGURE 2. Representative grids in the cylindrical and wake zones in the vicinity
of the cylinder.

the spanwise direction. The total number of grid points used to generate the grids in
the two zones was 2 941 920.

At the zonal boundaries, the two zones interface along common grid lines, thus
reducing the information transfer procedure from a two- to a one-dimensional
interpolation. For example, the upper zonal boundary of the cylindrical grid coincides
with an inner grid line in the wake grid. However, the grid points along this common
grid line do not coincide. A similar situation exists at the other zonal boundaries.

The boundaries that contain the cylindrical grid and the wake grid can be broadly
classified as natural and zonal boundaries. The natural boundaries include the circular
outer boundary of the cylindrical grid, the surface of the cylinder, the exit boundary
of the wake grid, the segments of the upper and lower boundaries of the wake
grid labelled as 'external boundary' in figure 1, and the boundaries in the spanwise
direction. The upstream segment of the upper boundary between the cylindrical and
wake grids is an example of the zonal boundaries used in the computation. Both the
natural and zonal boundary conditions used in this study are discussed in Rai (2008).

3. Results

The cylinder computation was performed at a Mach number of 0.1 and a Reynolds
number of 3900 based on free-stream velocity and the diameter of the cylinder.

The initial transients were eliminated by integrating the governing equations over a period of time corresponding to over 30 vortex-shedding periods. Each period corresponds to about 1600 time steps. The final turbulence statistics and velocity spectra were obtained over approximately 49 shedding periods ($TU_\infty/D = 234.4$ and 78 400 time steps). Here we first look at the velocity spectra and disturbance growth rate in the shear layer followed by an extensive exploration of the very near wake to better understand intermittency and compare these findings with those of Kim & Choi (2001), Prasad & Williamson (1997) and Wei & Smith (1986). Wake turbulence statistics and centreline velocity spectra obtained in the current computation are compared with experimental data by Rai (2008) and are not presented here.

3.1. *Detached shear-layer energy spectra and disturbance amplitude growth rates*

Shear-layer vortices play an important role in the evolution and eventual breakdown of the shear layers. They contribute to velocity fluctuations, within and outside the shear layer, occurring over a range of frequencies that scale with the Reynolds number. Velocity spectra in the vicinity of the shear layer (on the free-stream side) show sharp peaks at the shedding frequency, twice the shedding frequency and an additional broadband peak. The frequency at which this broadband peak occurs (ω_{SL}) is referred to as the shear-layer frequency and serves to characterize the entire range of frequencies that constitute the broadband peak. A power-law fit (ω_{SL}/ω_{st} versus Re) to the available experimental data (from numerous experiments conducted in as many experimental facilities) is provided in Prasad & Williamson (1997). This power-law relationship for Reynolds numbers between 1200 and 50 000 is given by

$$\omega_{SL}/\omega_{st} = 0.0235 \, Re^{0.67}.$$

The time variation of the streamwise velocity component was stored at three locations during the DNS to permit the calculation of velocity spectra. The streamwise locations of these points (A, B and C) are very nearly $x/D = 0.7$, 1.0 and 1.3, respectively. These locations relative to the shear layer are provided in a few of the figures that appear later in the text (e.g. figures 6 and 7).

Figure 3 shows the spectrum obtained at each location (averaged over the spanwise direction) and the value of ω_{SL}/ω_{st} (5.985) computed from the power-law fit of Prasad & Williamson (1997). The sharp peaks at the shedding frequency and the broadband peak at the shear-layer frequency are evident at all three locations. As in Unal & Rockwell (1988), there is no evidence of a subharmonic of the shear-layer frequency. However, the experiments of Rajagopalan & Antonia (2005) at $Re_D = 7410.0$ and 11 850.0 show spectral peaks at $\omega_{SL}/2$, thus indicating vortex pairing within the shear layer. They also observed a variation in the measured subharmonic frequency. Additional research is required to shed light on this matter. Here the computed value of ω_{SL}/ω_{st} (5.71) at $x/D = 0.7$ is in good agreement with the power-law fit. Further downstream, at $x/D = 1.0$ and 1.3, the broadband peak occurs at a slightly lower value of ω_{SL}/ω_{st} (5.14). A computed value of ω_{SL}/ω_{st} of 7.33 is reported in Dong *et al.* (2006) for the case $Re_D = 3900$. The broadband nature of the peak at ω_{SL} and its relation to the rate at which shear-layer vortices are generated deserves attention and is discussed in greater detail later in the text.

On the basis of earlier free shear-layer experiments which showed that the rate of growth of disturbances remains close to exponential with changing forced disturbance amplitude levels, Unal & Rockwell (1988) observe that even though the disturbance amplitudes in the cylinder detached shear layer are relatively large, linear stability theory should be able to provide a reasonable approximation to the growth of these
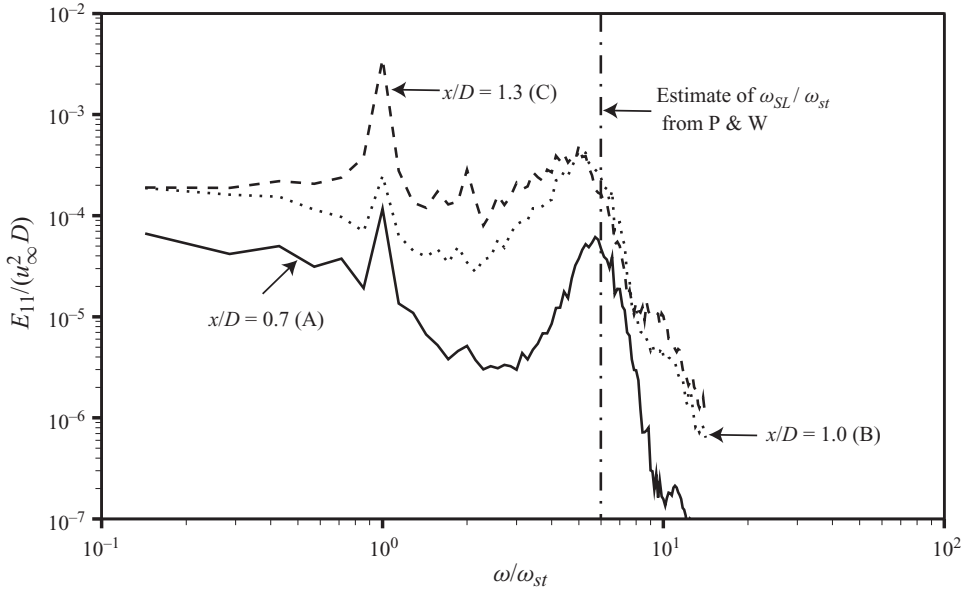
FIGURE 3. Spectrum (E_{11}) obtained in the vicinity of the shear layer. P & W denotes Prasad & Williamson (1997).
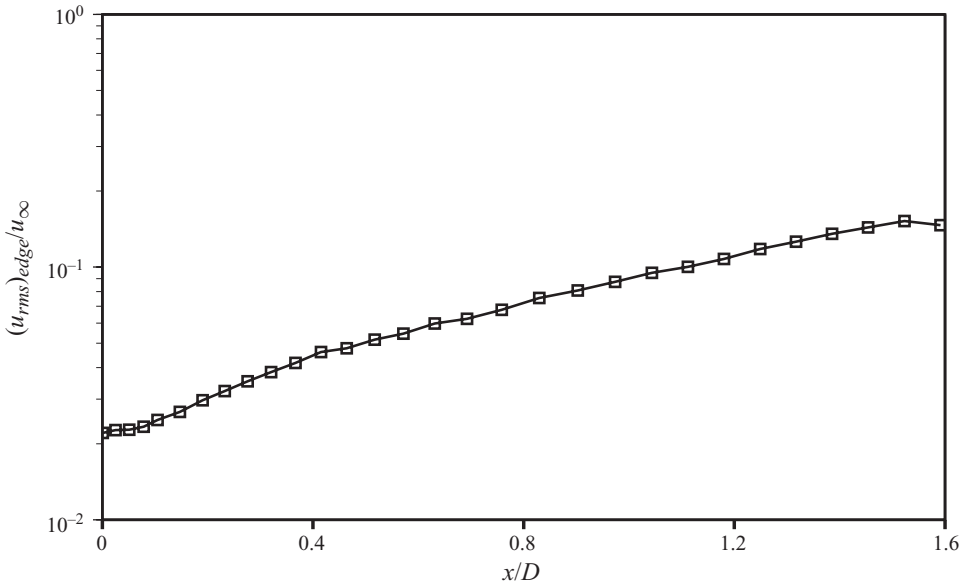

FIGURE 4. Variation of the amplitude of the fluctuating component of the streamwise velocity along the outer edge of the shear layer.

disturbances. Their experimental data for the detached shear layer indeed show a variation of disturbance amplitude with streamwise distance that is very nearly exponential. Here, as in Unal & Rockwell (1988), we examine the fluctuation level in the streamwise component of the velocity at the edge of the shear layer (on the free-stream side) as a function of streamwise distance. The fluctuating amplitude normalized by the free-stream velocity is plotted as a function of x/D in figure 4.

It should be noted that because these values were obtained at the edge of the shear layer, the corresponding data points lie on a curve. However, this curve is for the most part aligned with the x-axis. The region $0.3 \leqslant x/D \leqslant 1.5$ shows an exponential growth rate. The curve flattens after $x/D = 1.5$; this trend is also observed for large x/D in Unal & Rockwell (1988). The curve deviates slightly from exponential for $x/D < 0.3$. This deviation seems to be present even in the experimental data of Unal & Rockwell (1988) for the large Reynolds number cases, although the scale of the figures makes it difficult to ascertain this information. The slight departure from exponential is probably because of the proximity of this region to the point where the boundary layer separates to form the detached shear layer.

3.2. *Shear-layer intermittency*

Prasad & Williamson (1997) observe that the shear-layer instability manifests itself only intermittently, despite the fact that the velocity spectra in the vicinity of the shear layer show a distinct peak at the shear-layer frequency. They observe that Kármán vortex formation alone cannot explain intermittency because it has been observed even when Kármán vortices are suppressed. They also found that the shear-layer instability in their experiments was often observed to be in-phase across the wake. Additionally, they make a number of hypotheses that are pertinent to the present study, which are summarized here (all of them pertain to their parallel shedding case). (i) The random streamwise motion of the transition point caused by temporal changes in near-wake three-dimensional structures results in intermittency. (ii) Temporal variations in the velocity, because of Kármán vortex formation and the slight oscillation of the point of separation of the shear layer caused by this vortex formation, result in variability in the momentum thickness and thus variability in the most unstable frequency. This results in a broadband peak in the velocity spectra. (iii) The amplitude of shear-layer fluctuations can be classified into two groups, those that are large in comparison to Kármán vortex related fluctuations and those that are small. (iv) The 'in-phase' configuration is responsible for the large amplitude shear-layer fluctuations because of feedback between the two detached shear layers. They propose that a system consisting of two shear layers separated by a distance approximately of one cylinder diameter would admit a symmetric and an antisymmetric mode. They also suggest that a switching between the two modes would result in the time trace changing from large amplitude fluctuations to small amplitude fluctuations and vice versa. Here we investigate shear-layer intermittency and compare the findings with the above hypotheses.

Figure 5 shows the velocity time traces at point A at 20 % and 88.3 % span ($k = 13$ and 54, where k is the grid index in the spanwise direction) for the time steps 45 000–75 000. Both Kármán vortex fluctuations (quasi-periodic) and intermittency related fluctuations are observed in this figure. Because of features which are not evident in this figure, but will be apparent in later figures, it seems reasonable to classify shear-layer fluctuations (not including Kármán vortex related fluctuations) firstly as those that exhibit a distinct growth in amplitude followed by a subsequent reduction in amplitude (class A) and a second category that exhibits relatively smaller changes in amplitude that are harder to discern (class B). Based on the time trace at $k = 13$, class A can be further classified (preliminary) as class A_1 which includes waves of peak amplitude 1.5–4 times as large as the Kármán fluctuations, and class A_2 which consists of waves 0.25–1.5 times as large in amplitude (this classification is similar to that of Prasad & Williamson 1997). A more precise characterization of this class is provided later. Class A fluctuations are clearly observed in figure 5. Class B
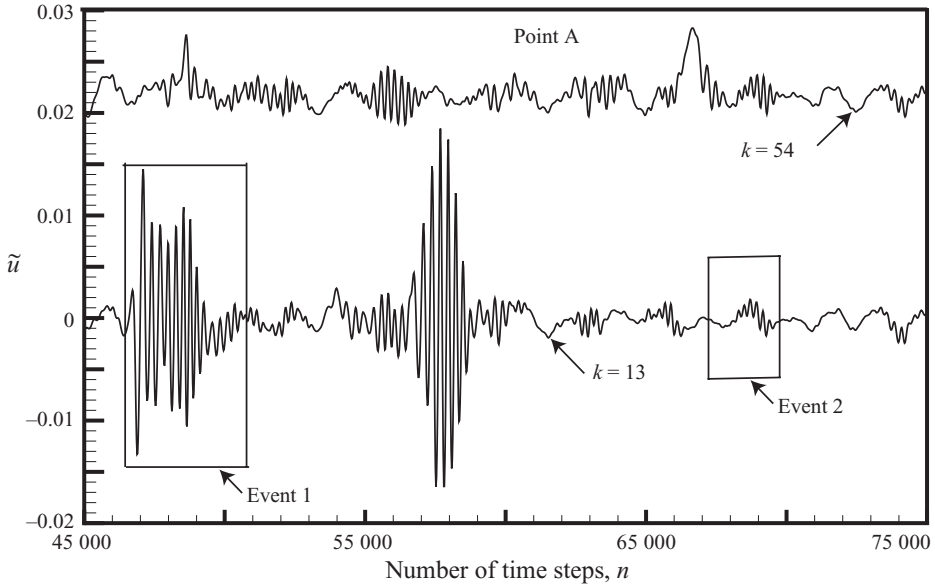
FIGURE 5. Fluctuating component of the streamwise velocity at $x/D = 0.7$
($n = 45\,000,\ 75\,000$).

fluctuations are barely discernible but will become apparent in later figures. Figure 5 provides a confirmation of intermittency via computations, they are present as far upstream as $x/D = 0.7$, where the cross-stream motion of the shear layer is small (they are even observed at $x/D = 0.3$).

This period in time (45 000–75 000) was chosen because of the clear separation between the different classes. Event 1 contains a member of class A_1. The rapid growth and subsequent decay in the amplitude of the time trace is apparent. The peak amplitude is several times as large as that associated with Kármán vortex formation (an estimate of shedding amplitudes can be obtained from the trace around $n = 72\,000$). Event 2 in figure 5 contains a member of class A_2. The amplitude of fluctuations is about the same as those resulting from Kármán vortex shedding. Figure 5 also includes the time trace from $k = 54$ which shows very little effect of the large disturbance at $k = 13$, thus demonstrating the localization of this event in the spanwise direction and is similar to the three-dimensional instability mentioned in Kim & Choi (2001).

Event 1 begins at approximately $n = 46\,400$. Instantaneous spanwise vorticity contours in the (x, y) plane at $k = 13$ are now used to visualize the evolution of the detached shear layer in time. Figure 6 shows contours at $n = 46\,400$. The interaction of the upper shear layer with an ingested vortex (clockwise rotation, obtained during the shear-layer breakdown process) is evident. The ingested vortex is marked by a blue arrow. The interaction results in an inflection in the shear layer at about $x/D = 1.4$ causing it to tilt upward and reach a maximum height at about $x/D = 1.9$. The shear layer subsequently descends. It will become apparent in later figures that this effect is localized in the spanwise direction.

Figure 7 shows vorticity contours at $n = 46\,850$. The interaction seen in figure 6 is followed by shear-layer breakdown that is evident in figure 7. The detachment of the downstream portion of the shear layer is clearly seen here. The beginning of a second separation at about $x/D = 0.7$ is also evident. Because of the proximity of these
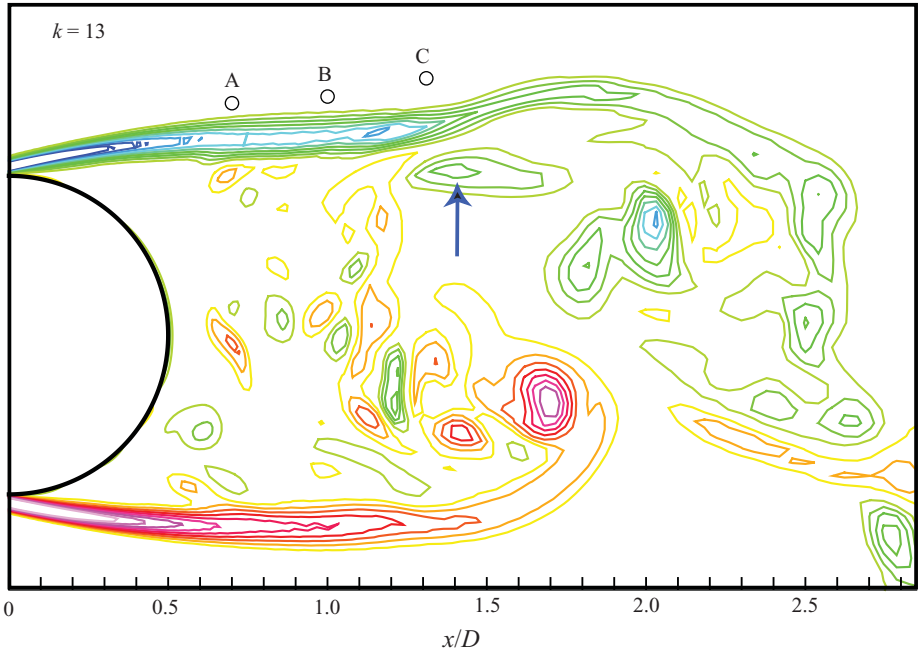
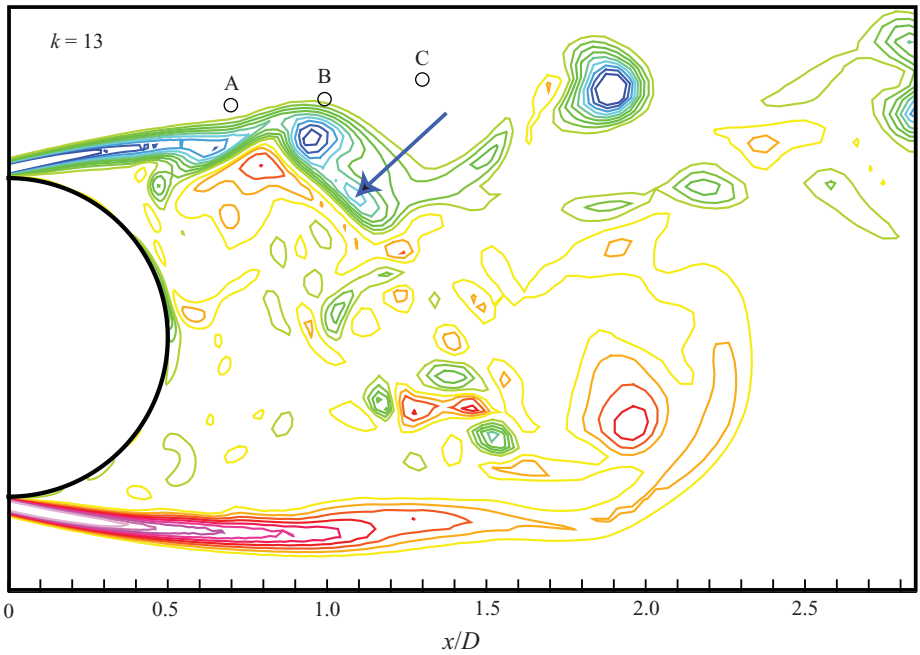FIGURE 6. Instantaneous contours of spanwise vorticity (Event 1, $n = 46\,400$).

FIGURE 7. Instantaneous contours of spanwise vorticity (Event 1, $n = 46\,850$).

events to points A, B and C, time traces at these locations all show large amplitude fluctuations. It was found that the breakdown process is followed by a short period in which the shear layer partially regenerates. This breakdown/regeneration cycle repeats itself a few times within Event 1. The shear layer fully regenerates at about
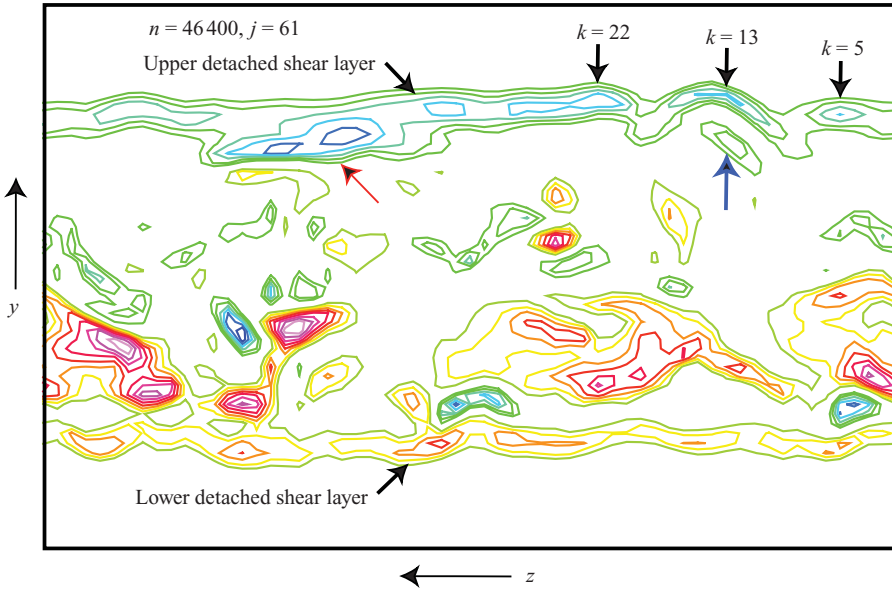
FIGURE 8. An end view (looking upstream) of instantaneous contours of spanwise vorticity.

$n = 50\,700$ (4300 steps, or about 2.7 Kármán shedding cycles after initiation). The computed results in figures 6 and 7 show that as stated in Prasad & Williamson (1997), signal intermittency is accompanied by the movement of the transition region upstream. However, the root cause is an interaction between the shear layer and wake vortices ingested by the recirculation region, and not simply temporal changes in the near-wake three-dimensional structures as suggested by them. The upstream movement of shear-layer transition is just one of the effects of the interaction. The lower shear layer is relatively calm during this period in which the upper one experiences massive disruption. Clearly, Event 1 is not an in-phase phenomenon and yet exhibits large-scale intermittency. Prasad & Williamson (1997) report that in the majority of instances the shear-layer instability is in-phase across the wake. This high frequency of occurrence of the in-phase instability was not observed. Event 1 as depicted in figures 6 and 7 is of course not an isolated incident. Additional class A_1 instances are presented later.

Figure 8 shows an end view (looking upstream) of instantaneous contours of spanwise vorticity on the surface $j = 61$ in the wake zone at $n = 46\,400$. The streamwise location of this surface is close to the arrow pointing to the ingested vortex in figure 6. The portion of this surface that is included in figure 8 is very nearly a constant x plane. Both the upper and lower detached shear layers are seen in this figure. The locations $k = 5$, 13 and 22 are marked by black arrows. The ingested vortex of figure 6 is marked by a blue arrow. The upward dislocation of the upper detached shear layer caused by its interaction with the ingested vortex is evident. The fact that this effect is localized in the spanwise direction is also evident. The elevated portion of the shear layer (near $k = 13$) is bounded by two depressed regions followed by slightly elevated regions near $k = 5$ and 22. These two regions of minor elevation are also caused by recirculation region vortices but of lower strength. The region marked by the red arrow was found, via spanwise vorticity contours in an (x, y) plane, to be the precursor to another breakdown event.
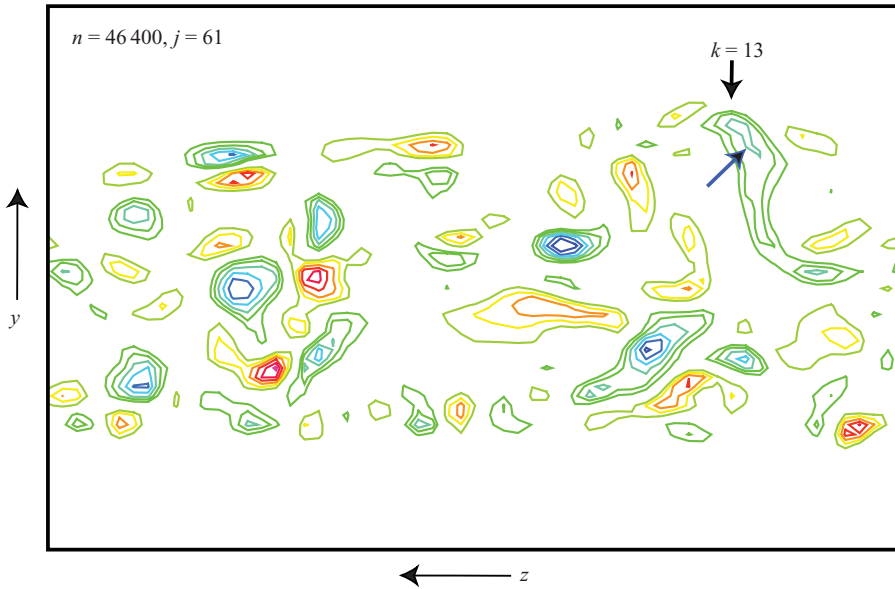
FIGURE 9. An end view (looking upstream) of instantaneous contours of streamwise vorticity.

Figure 9 shows instantaneous contours of streamwise vorticity on the same surface as in the previous figure at $n = 46\,400$. Although several vortex pairs are clearly visible in the recirculation region, in the proximity of the shear-layer inflection at $k = 13$ only a single region of concentrated streamwise vorticity (negative, marked by a blue arrow) is seen (although it is flanked by two regions of weak positive streamwise vorticity, seen as closed green contours). This concentration of negative streamwise vorticity also contributes to the localized elevation of the shear layer. Although, as concluded in Kim & Choi (2001), a strong counter-rotating pair of vortices could generate a three-dimensional instability, we see here that the presence of a region of sufficiently strong streamwise or spanwise vorticity, or a combination thereof, in the vicinity of the shear layer can also result in a deformation of the layer and subsequently, shear-layer instability. A second point to be noted is that almost all of the regions of streamwise vorticity are found between the two shear layers, with several lying adjacent to the shear layers but not confined to these layers. This lack of streamwise vorticity within the shear layer is in apparent contrast to the expectation of Wei & Smith (1986) of shear-layer vortices that undergo stretching in the streamwise direction by the Kármán vortices and thus producing a streamwise component. However, a careful look at vortical structures within the shear layer in the following figures shows several streamwise vortex pairs present. These pairs are generally much weaker than the ones seen in figure 9.

Figure 10 shows instantaneous contours of the fluctuating component of the spanwise vorticity (ω'_z) on a surface contained within the shear layer. The surface was defined as consisting of those points within the shear layer at which the instantaneous streamwise velocity was half the free-stream velocity. The mean value of vorticity, at any given point on this surface, which is used to compute the fluctuating component of vorticity was obtained from creating a similar surface with the mean flow. Since shear-layer vortices result in vorticity levels that are perturbations of the mean vorticity at any given point within the shear layer, contours of ω'_z can be used to depict the presence and structure of these vortices. Contours corresponding to $\omega'_z = 0$ were not
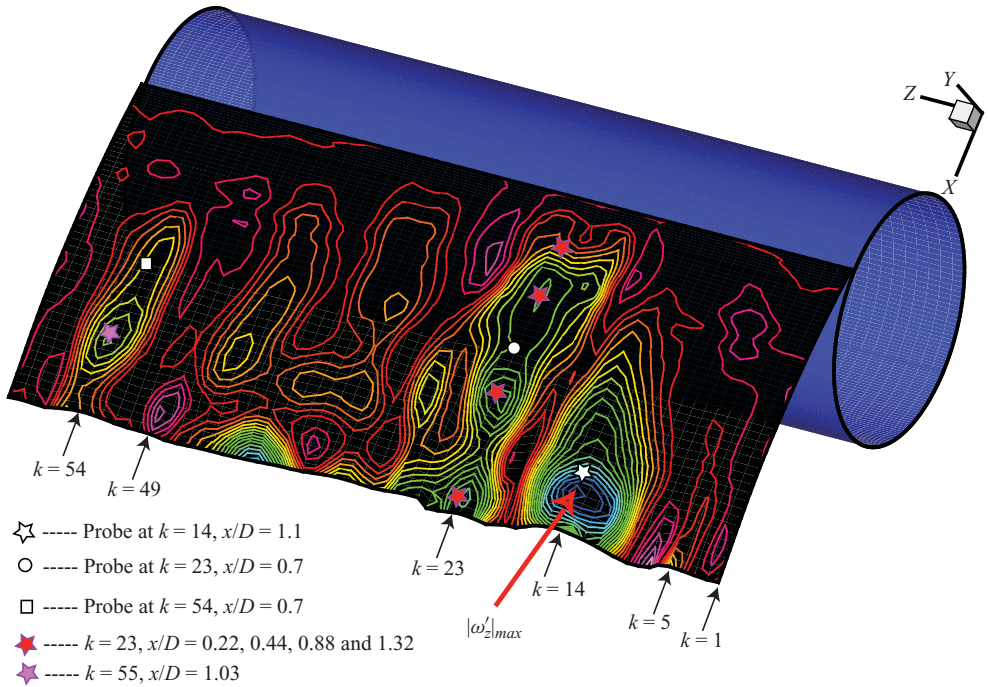
FIGURE 10. Instantaneous contours of fluctuating spanwise vorticity in the shear layer ($n = 46\,400$).

plotted to accentuate the separation between regions of positive and negative ω'_z. The cellular regions corresponding to the shear-layer vortices that were observed in Wei & Smith (1986) are apparent. The multiple-vortex structure along the $k = 23$ line shows three of them stacked in the streamwise direction (patches of yellow and green, approximately centred at the red stars). There are five such stacks of cells in this figure, two prominent ones are located near the lines $k = 14$ and 54. At $k = 14$, the shear-layer vortices seem to have almost merged together. As seen earlier in figures 6 and 7, the shear layer is near breakdown at this point in time at $k = 13$. The region of strong vorticity marked by the red arrow at $k = 14$ is a precursor to shear-layer breakdown. Figure 10 also shows a few regions of positive ω'_z (magenta) which bear some resemblance to the shear-layer vortices. However, side views (x, y planes) at the appropriate spanwise locations (e.g. $k = 7$) only show a more diffuse shear layer.

The undulating structure of the shear layer can be observed in figure 10. The upward dislocation of the shear layer in the vicinity of $k = 14$ is clearly visible. Figure 11 shows contours of instantaneous shear-layer elevation on the same surface as in figure 10. In general, the regions of negative perturbation vorticity (yellow/green/blue patches) in figure 10 coincide with regions that are positively dislocated, and the regions of positive perturbation vorticity (red/magenta patches) coincide with regions that are negatively dislocated. This leads to the conjecture that in a relatively quiescent period when the shear layer is intact and the principal curvature of the surface is in the spanwise direction, the shear-layer vortices with their associated spanwise vorticity undergo vortex stretching in regions of positive elevation (negative curvature) and compression in regions of negative elevation (positive curvature). This would result in shear-layer vorticity amplification in regions of positive elevation. The combined effects of amplified negative shear-layer
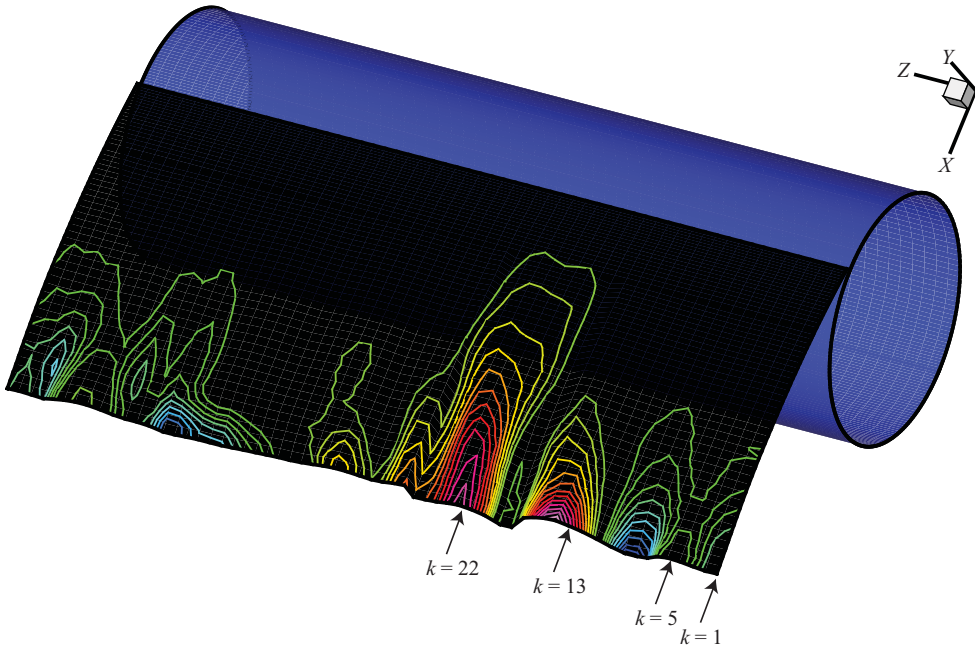
FIGURE 11. Instantaneous contours of elevation (y_{SL}) in the shear layer ($n = 46\,400$).

vorticity and positive elevation (closer proximity to probes outside the shear layer) would then explain the intermittency observed initially in the velocity signal. Subsequent shear-layer breakdown/regeneration cycles would result in later stage intermittency in the signal followed by a relatively quiescent signal when the shear layer regenerates substantially. However, it still remains to be seen if the intermittent velocity fluctuations outside the shear layer are closely correlated to the vorticity associated with the passing shear-layer vortices. Data substantiating this correlation are provided later.

Figure 12 shows instantaneous contours of streamwise vorticty on the same surface as the previous two figures. Three pairs of counter-rotating vortices are observed straddling the line $k = 23$, at the locations $x/D = 0.22$, 0.88 and 1.32. These points are marked by red stars in figures 10 and 12. From these two figures it is observed that the latter two points also correspond to regions of concentrated spanwise vorticity. The point at $x/D = 0.22$ is discussed in the following paragraphs. Streamwise vortex pairs are also observed straddling the location $k = 55$, $x/D = 1.03$ (marked by a magenta star in both figures) and the point at which $|\omega'_z|_{max}$ occurs. Again we have regions of concentrated spanwise vorticity straddled by regions of concentrated positive and negative streamwise vorticity, on the right and left, respectively. Instantaneous contours of cross-stream vorticity on the same surface as the previous figures are plotted in figure 13. Here we have large elliptical patches of negative cross-stream vorticity to the right of the points of interest (marked by red and magenta stars as in figures 10 and 12) and positive cross-stream vorticity to the left of these points. The vorticity contours of figures 10, 12 and 13 clearly indicate the presence of the three-dimensional cellular vortex structure first reported in Wei & Smith (1986). A sketch of a typical cellular vortex is shown in figure 13. Figures 10, 12 and 13 indicate that the vertex of the hairpin structure lies on the ridge of the elevated shear layer and the legs are located in the valleys on either side of the ridge.
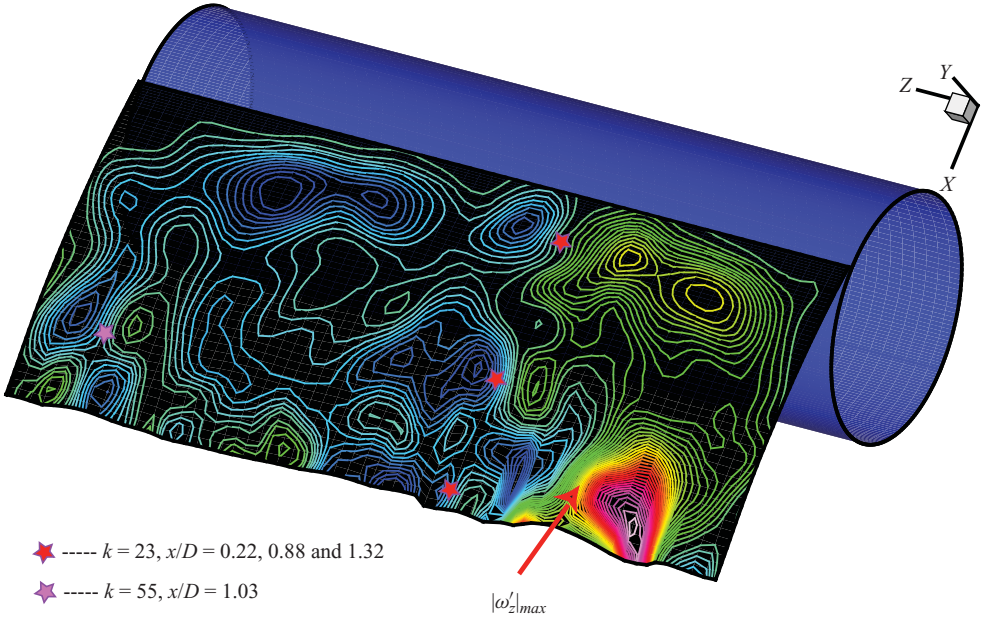
FIGURE 12. Instantaneous contours of streamwise vorticity in the shear layer ($n = 46\,400$).
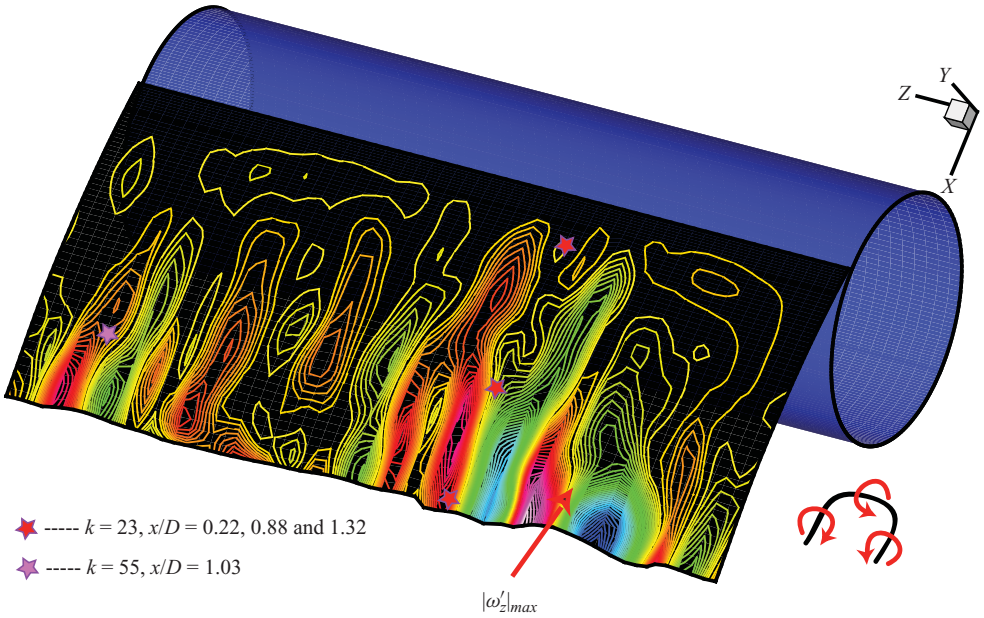

FIGURE 13. Instantaneous contours of cross-stream vorticity in the shear layer ($n = 46\,400$).

The location $k = 23$, $x/D = 0.22$ sheds light on the generation of perturbations in the shear-layer vorticity. Figure 14 shows instantaneous contours of spanwise vorticity in the (x, y) plane $k = 13$ at $n = 46\,400$. The vorticity range in which the contour levels are plotted is approximately one-fifth of that used in figure 6 to accentuate relatively weaker recirculation region vortices. Contour levels close to zero were not plotted to
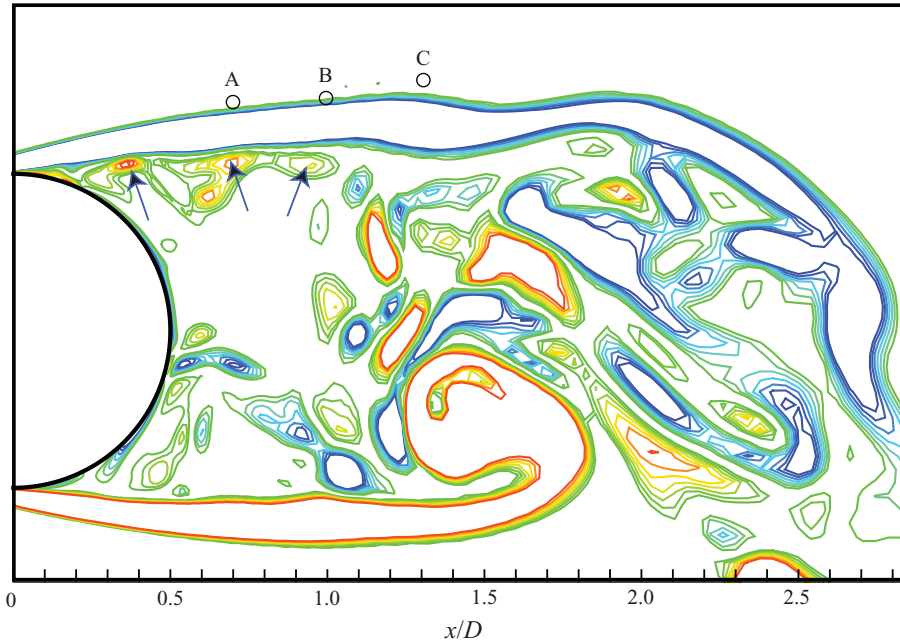
FIGURE 14. Instantaneous contours of spanwise vorticity in the (x, y) plane at $k = 23$ $(n = 46\,400)$.

reduce clutter. This strategy results in regions devoid of contours where one would normally expect contours, but it also clearly depicts the recirculation region vortices (marked by blue arrows) interacting with the upper shear layer in the vicinity of the base of the cylinder $(0.2 < x/D < 0.9)$. The resulting changes to the shape of the shear layer are evident from figure 14. Here we make the case that these interactions result in the generation and initial amplification of spanwise and streamwise vorticity.

Assume that the shear layer is initially quiescent, that the flow is essentially two-dimensional in a region near the base (spanwise velocity and spanwise derivatives of all the flow variables are zero) and that the shear layer undergoes a rapid but small and localized upward dislocation that is centred at some spanwise location (z_d). We further assume, without loss of generality, that the disturbances caused are either symmetric (as in the case of streamwise velocity) or antisymmetric (spanwise velocity) in z about the plane $z = z_d$. At $z = z_d$, we then have $w = 0$, $\partial u/\partial z = 0$, $\partial v/\partial z = 0$, $\omega_x = 0$ and $\omega_y = 0$ for $t \geqslant 0$. Consider the inviscid, incompressible form of the vorticity transport equation, for the spanwise vorticity component:

$$\frac{\mathrm{D}\omega_z}{\mathrm{D}t} = \omega_x \frac{\partial w}{\partial x} + \omega_y \frac{\partial w}{\partial y} + \omega_z \frac{\partial w}{\partial z}. \tag{1}$$

In the plane $z = z_d$ this equation reduces to

$$\frac{\mathrm{D}\omega_z}{\mathrm{D}t} = \omega_z \frac{\partial w}{\partial z}. \tag{2}$$

The spanwise vorticity ω_z is negative in the upper shear layer. The upward dislocation of the shear layer causes the spanwise velocity to be negative for $z < z_d$ and positive for $z > z_d$ in the vicinity of z_d (efflux of fluid away from the plane $z = z_d$). This is
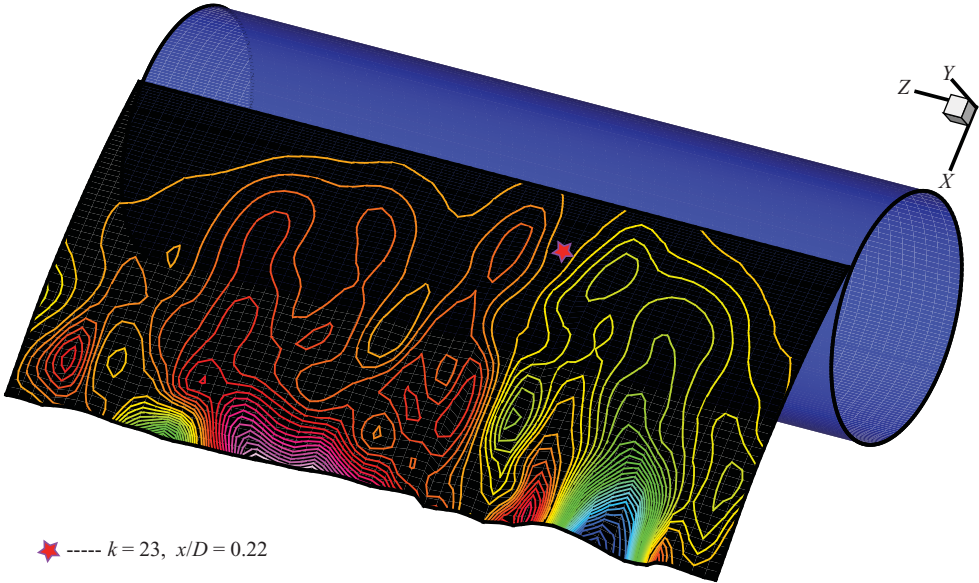
----- $k = 23$, $x/D = 0.22$

FIGURE 15. Instantaneous contours of spanwise velocity in the shear layer ($n = 46\,400$).

clearly seen in figure 15, which shows instantaneous contours of the spanwise velocity within the shear layer. The red star marks the location $k = 23$, $x/D = 0.22$.

Contour lines corresponding to $w = 0$ have been omitted to clearly delineate regions of positive and negative w (one such $w = 0$ contour passes through the star). This distribution of spanwise velocity (figure 15) results in $\partial w/\partial z > 0$ at $z = z_d$. This in turn results in the right-hand side of (2) being negative and thus local amplification of spanwise vorticity in this plane or the appearance and growth of shear-layer vortices.

We now consider the counter-rotating pair of streamwise vortices straddling the location $k = 23$, $x/D = 0.22$ in figure 12. The inviscid, incompressible form of the vorticity transport equation for the streamwise vorticity component is given by

$$\frac{D\omega_x}{Dt} = \omega_x \frac{\partial u}{\partial x} + \omega_y \frac{\partial u}{\partial y} + \omega_z \frac{\partial u}{\partial z}. \tag{3}$$

Prior to the dislocation, all of the terms on the right-hand side of (3) are zero because the x and y vorticity components and the spanwise derivatives are all zero in the region of interest. Immediately after the dislocation, the third term on the right-hand side becomes non-zero. This is because ω_z within the shear layer is large and, while $\partial u/\partial z$ is small, it is finite. Note that the magnitude of the term $\partial u/\partial z$ on either side of the ridge, in the spanwise direction, can be approximated as $-\theta \omega_z$. This is a result of the gradient of u in the y-direction in the unperturbed shear layer, being partially converted into a gradient in the z-direction because of the deformation of the shear layer (θ is the angle subtended between the quiescent shear layer and the dislocated shear layer in an end view). Here we have also assumed that $\partial v/\partial x$ is small in magnitude compared to the term $\partial u/\partial y$. Additionally,

$$\left.\begin{array}{ll} \dfrac{\partial u}{\partial z} < 0, & z < z_d, \\[2mm] \dfrac{\partial u}{\partial z} > 0, & z > z_d \end{array}\right\} \tag{4}$$

in the vicinity of the dislocation. The conditions given in (4) combined with (3) (with only the third term on the right-hand side included) result in the generation of a region of positive ω_x for $z < z_d$ (right of the dislocation in figure 12) and a region of negative ω_x for $z > z_d$ (left of the dislocation). This is substantiated by the pair of counter-rotating streamwise vortices straddling the line $k = 23$ in the vicinity of $x/D = 0.22$ (and at all the other points marked by stars in figure 12). The necessary dislocation for this case is caused by the interaction between the recirculation region vortices and the shear layer seen in figure 14. The continued evolution of the pair of streamwise vortices later in time is not as easily obtained analytically. In fact, the first two terms on the right-hand side of (3) have the opposite sign to the third term and are significant in magnitude. However, at the centres of the streamwise vortices seen in figure 12, it was found that the third term was substantially larger in magnitude than the sum of the magnitudes of the first two terms, thus causing continued growth of these vortices. This explains the appearance of spanwise waviness in the essentially spanwise shear-layer vortices initially, and later the hairpin vortices of figure 13.

The upward dislocation of the upper shear layer serves the dual purpose of initially generating spanwise and streamwise vorticity in this shear layer and strengthening existing shear-layer vortices, thereby hastening the transition process. Thus, the shape of the shear layer plays a critical role in the evolution of shear-layer vortices as well as in its own continued evolution.

The evidence provided thus far to demonstrate that signal intermittency is caused by the strengthening of shear-layer vortices has been qualitative in nature. A direct quantitative link between the strength of shear-layer vortices and signal intermittency is required for a more convincing argument. While the data at points A, B and C were stored continuously in the 49 shedding period computation, the full three-dimensional dataset was only stored sporadically. In order to thoroughly investigate the instability mechanisms, more comprehensive data are required at frequent time intervals. Hence, the computation was continued past the original 49 cycles and a more comprehensive dataset was stored over 20 cycles of this extended computation. The figures presented from here onwards are from this extended computation.

Figure 16 shows fluctuating velocity and vorticity signals obtained at point B at $k = 1$. All the signals have been filtered using a high-pass filter, with the cutoff frequency set to 2.25 times the Strouhal frequency to eliminate fluctuations related to Kármán vortex shedding and those at even lower frequencies. Figure 3 shows that shear-layer vortex related fluctuations occur at frequencies greater than 2.25 times the shedding frequency; thus, the cutoff frequency used here is appropriate. The signal at the bottom of the figure is the fluctuating streamwise velocity component at point B. The rest of the signals (four) are the fluctuating spanwise vorticity at various points within the shear layer (underneath point B). Together these four points span the width of the shear layer. The uppermost one in the figure is adjacent to the recirculation region and the lowermost one to point B.

The shear-layer vortices passing under point B result in fluctuations in the vorticity traces in figure 16. All four of the vorticity traces show intermittent behaviour, clearly demonstrating that intermittency is a real independent phenomenon and not simply an observation that is a result of the cross-stream motion of the shear layer. The multiple spikes within a period of intermittency are caused by the many shear-layer vortices passing by this location. The relatively large fluctuations in the third vorticity signal are because the corresponding location is near the middle of the shear layer and thus experiences the passage of the vortex cores. The vorticity signals at locations 1–3 are well correlated. The vorticity signal closest to the recirculation region is
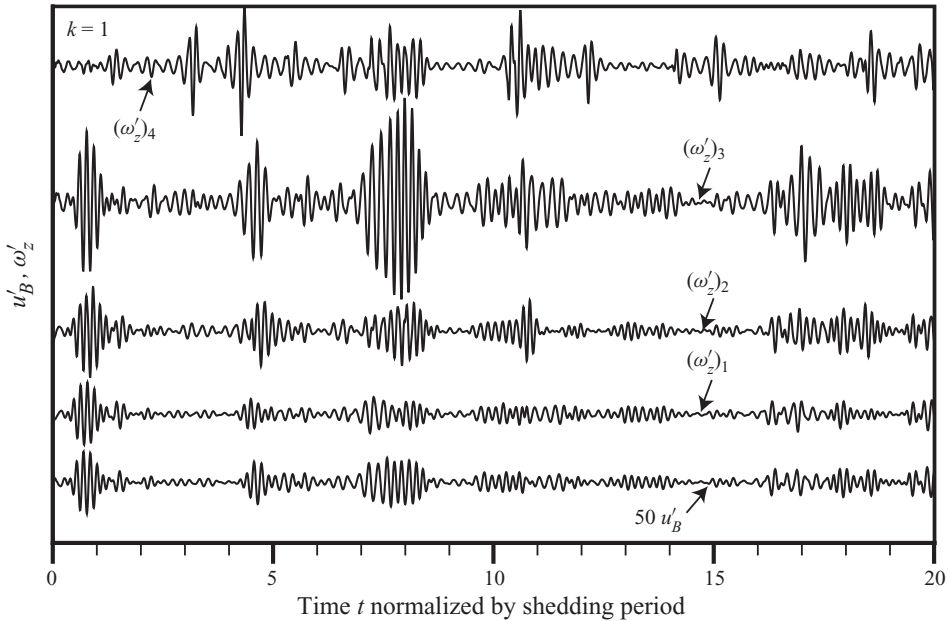
FIGURE 16. Filtered fluctuating component of streamwise velocity (point B) and spanwise
vorticity (across shear layer in the vicinity of point B).

perhaps not as well correlated with the rest of the signals because of its exposure
to the recirculation region and ingested vortices. The intermittent periods in the
velocity signal are closely correlated with those in the vorticity signals. In general,
the magnitudes are also well correlated. This establishes the cause/effect relationship
between the vorticity and velocity signals. Thus, experimentally observed velocity
intermittency outside the shear layer is caused by intermittent shear-layer vortices.
Any movement of the shear layer towards the observation point results in higher
velocity amplitudes.

A computational investigation of the instability of the shear layer is presented
in Kim & Choi (2001). Time traces of streamwise velocity and contours of the
fluctuating component of the streamwise velocity in a plane corresponding to the
spanwise direction and time ($t–z$ plane) in the vicinity of the shear layer are presented.
Three-dimensional vortex structure in the shear layer and wake is also discussed.
They propose the presence of two distinct types of shear-layer instabilities: one
which is three-dimensional and is generated locally by a strong streamwise vortex
pair underneath the shear layer, and another which is quasi-two-dimensional and is
related to Kármán vortex shedding. It is observed that the latter instability is caused
by a disorder in Kármán vortex shedding and appears in phase in the two detached
shear layers.

Figure 17 shows contours of u' at the point $x/D = 1.0$, $y/D = 0.75$ (point B in
figure 6) in the ($t–z$) plane, that is, the variation of u' in time at all the grid points in
the spanwise direction corresponding to location B. This figure also shows a similar
plot at $x/D = 1.0$, $y/D = -0.75$, which is a point whose location with regard to the
lower shear layer is identical to that of point B to the upper shear layer. The time
period corresponds to the first 10 Kármán shedding cycles of figure 16. The spanwise
extent corresponds to the entire computational domain in that direction. This figure is
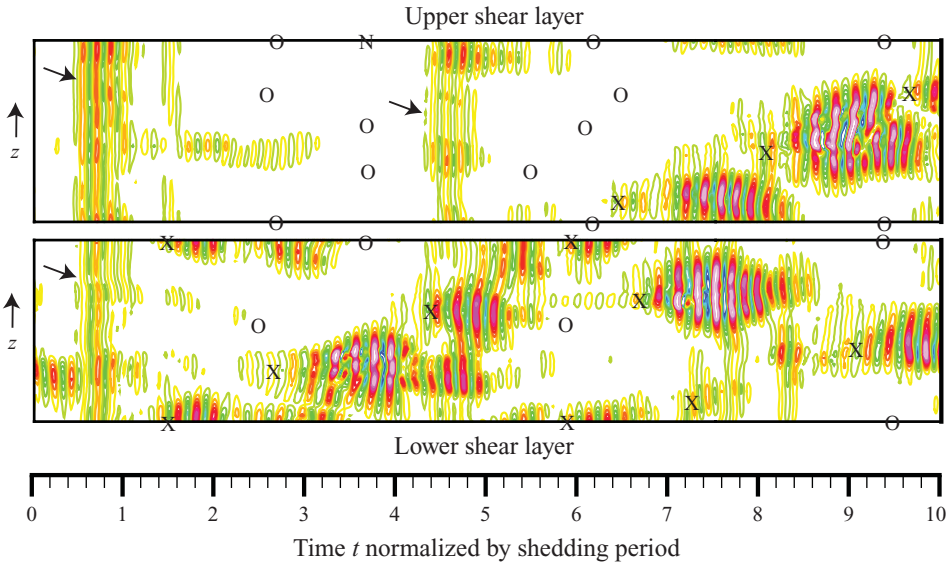similar to the one provided in Kim & Choi (2001) but contains information from both

FIGURE 17. Instantaneous contours of fluctuating streamwise velocity in a (t, z) plane at probe B over a period of 10 shedding cycles.

the shear layers. There the (t, z) plane was found to be populated with two types of contour distributions: one consisting of vertical bands of contours running the entire width of the domain and the other consisting of bands which in some instances did not cover the entire width and in others covered the width but contained islands within. The first set was labelled a quasi-two-dimensional instability related to Kármán vortex shedding, and the second set was labelled a three-dimensional instability caused by pairs of counter-rotating streamwise vortices underneath the shear layer.

Here we find that although around $t = 0.6$ and 4.6 in the time period shown in figure 17 there exist what may be vertical bands running the width of the computational region, the majority of events are fully three-dimensional in nature. The one at 0.6 is seen in both the upper and lower shear layers as observed in Kim & Choi (2001). The time period over which the contours are depicted is large and hence figure 17 is a good indicator of all of the underlying instability processes. The breakdown process seen earlier in figures 6 and 7 is very similar to the large-scale three-dimensional breakdown events seen in figure 17.

The first observation to be made from this figure is that the large amplitude three-dimensional patches in the upper and lower shear layers are not well correlated. These events in the two shear layers are essentially independent of each other. However, vortices generated during the breakdown of one shear layer do affect the other shear layer. Secondly, contours of instantaneous spanwise vorticity in the (x, y) plane at all the points denoted by the letter 'O' showed the corresponding shear layer to be quiescent and free of any nearby ingested vortices. These locations were obtained by locating all the quiescent regions in a plot similar to that of figure 17, but with eight times as many contours. Figure 18 is an example of one such location showing a quiescent upper shear layer and the absence of ingested vortices near this shear layer. Thirdly, instantaneous spanwise vorticity in the (x, y) plane at all the points denoted by the letter 'X' showed the initiation of instability in the corresponding shear layer and one or more ingested vortices near the shear layer. Figure 19 is an example showing the upper shear layer interacting with four different vortices of the opposite
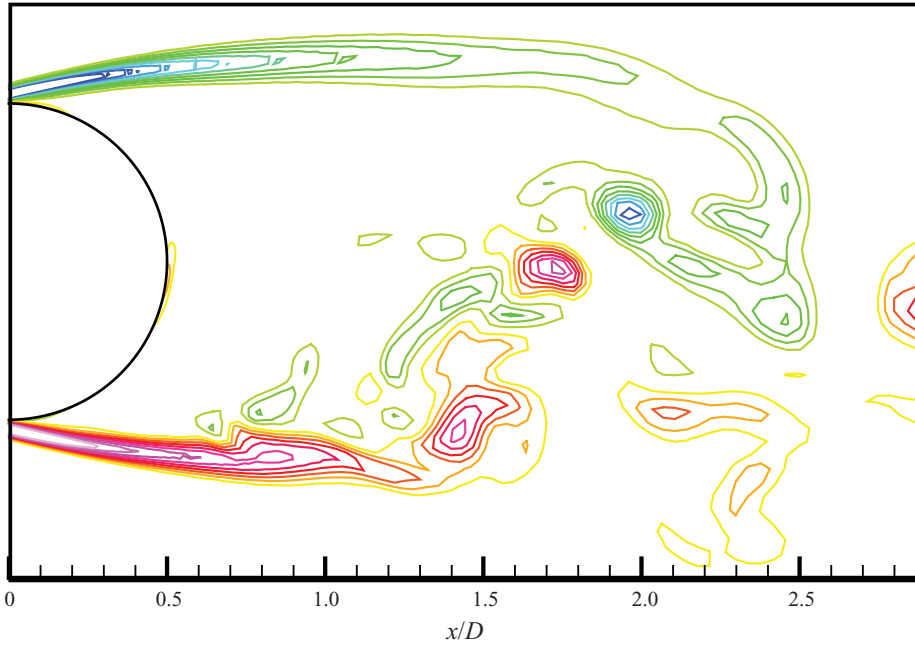
FIGURE 18. Instantaneous spanwise vorticity contours in the (x, y) plane at $k = 1$, $t = 2.6$.
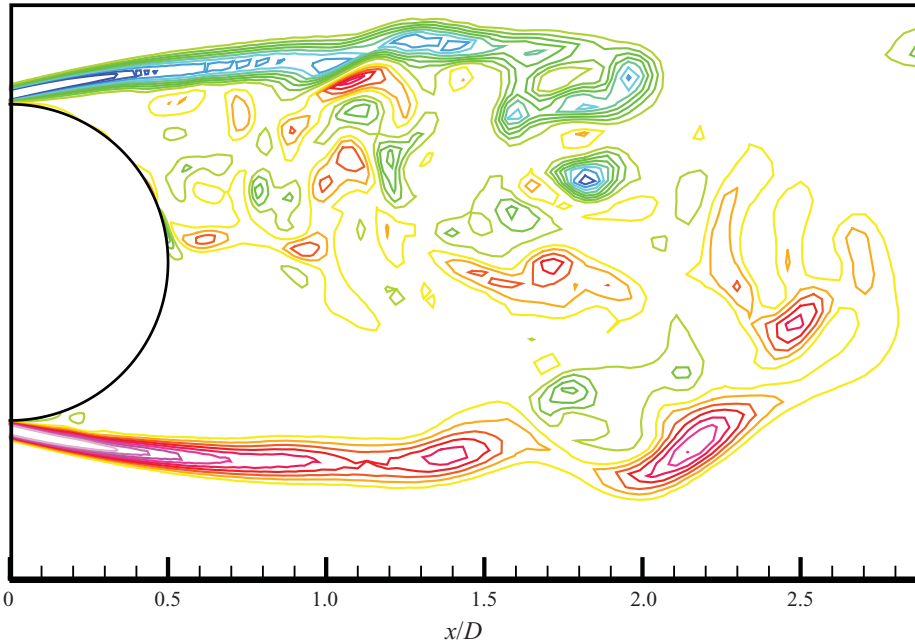

FIGURE 19. Instantaneous spanwise vorticity contours in the (x, y) plane at $k = 8$, $t = 6.4$.

sign and the generation of shear-layer vortices within the shear layer. An animation of the time period containing this event is available at journals.cambridge.org/flm. The point denoted as 'N' in the upper shear layer ($k = 61$, $t = 3.6$) showed multiple ingested vortices but a relatively quiescent state. Figure 20 shows instantaneous
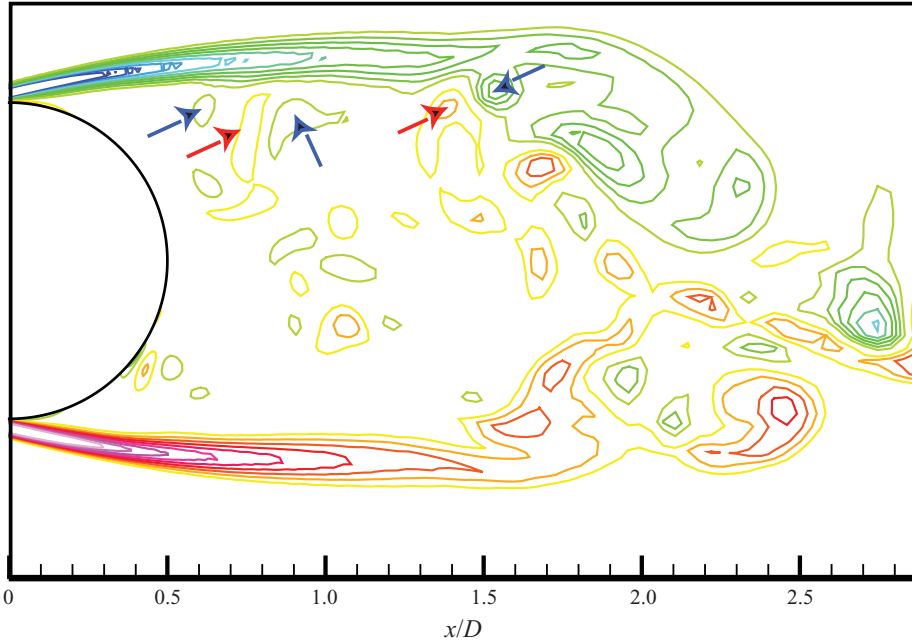
FIGURE 20. Instantaneous spanwise vorticity contours in the (x, y) plane at $k = 61$, $t = 3.6$.

spanwise vorticity in the (x, y) plane at this location. There are five different vortices interacting with the shear layer. The ones with negative vorticity are marked by a blue arrow and those with positive vorticity by a red arrow. The relatively undisturbed state of the shear layer can be explained by the opposing effect that positive and negative regions of vorticity have on the shear layer, the net effect being rather small. This event 'N' is relatively rare. The observations made above show that the interactions between ingested vortices and the shear layers are a major cause of intermittency.

In general, class A_2 events have shorter life spans (about one shedding period). Event 2 in figure 5 is a good example of this class. Another such event is also seen around $t = 0.6$ in figure 16. This latter event is observed in figure 17 as a band of contours spanning the computational region in the z-direction both in the upper and lower shear layers. Figure 21 shows instantaneous contours of fluctuating spanwise vorticity at $t = 0.45$ in the upper shear layer (initiation of instability). The seven stars show the first signs of shear-layer vortices at a particular streamwise location. A plot of instantaneous elevation of the shear layer as in figure 11 showed that there were as many raised regions as shear-layer vortices, and these regions correspond to the spanwise locations of the vortices. Contours of instantaneous spanwise vorticity in (x, y) planes also showed ingested vortices interacting with the shear layer at spanwise locations corresponding to the regions of positive elevation. These interactions occurred at different (x, y) locations at the different spanwise locations. The interacting vortices were not always the same vortex extended in the spanwise direction. These facts indicate that the seemingly two-dimensional instability consists of multiple, spanwise-stacked shear-layer vortices that are caused by interaction of the shear layer with multiple ingested vortices at about the same instant in time. Figure 22 shows fluctuating instantaneous spanwise vorticity within the upper shear layer at $t = 0.6$ (a little further into this particular event). The lower set of vortices, marked by stars, are the same as those seen in figure 21 but strengthened and located
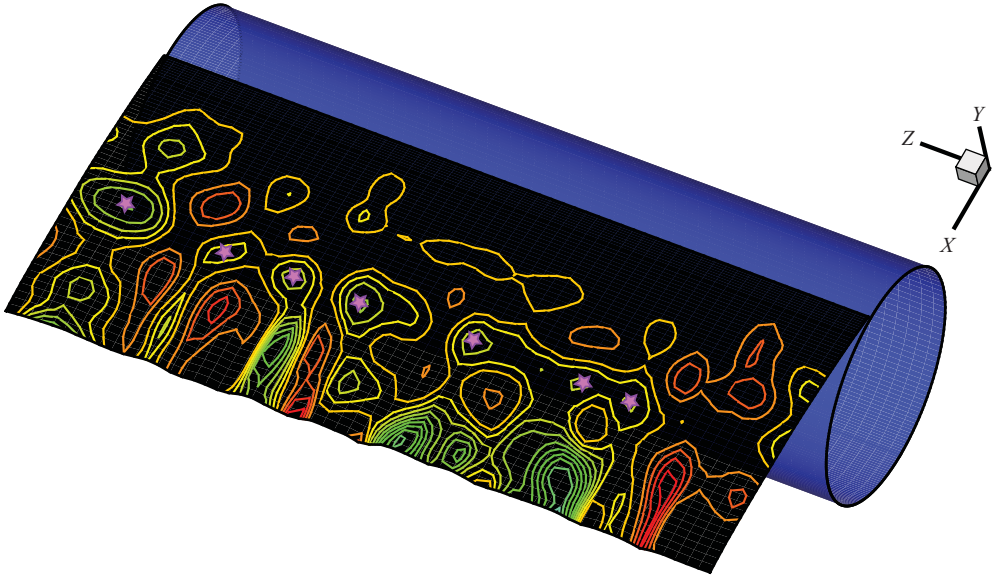
M. M. Rai

FIGURE 21. Instantaneous contours of fluctuating spanwise vorticity in the upper shear layer ($t = 0.45$).
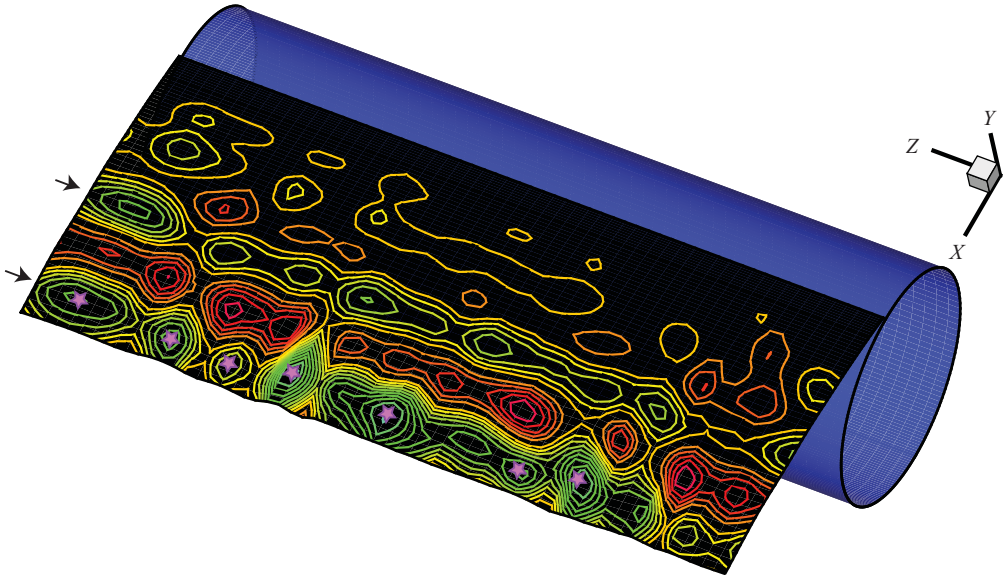

FIGURE 22. Instantaneous contours of fluctuating spanwise vorticity in the upper shear layer ($t = 0.60$).

further downstream. They have also spread in the z-direction and now abut each other. The set of vortices upstream are the next generation of shear-layer vortices and show the same general structure as the first in figure 21, but are more extended in the spanwise direction. Shear-layer vorticity contours as in figure 22, but for the lower shear layer at $t = 0.6$, are shown in figure 23. They do not show the same level of spanwise organization of vortices; the multiple spanwise-stacked vortex structure is conspicuous here. This feature is maintained throughout this event in the lower
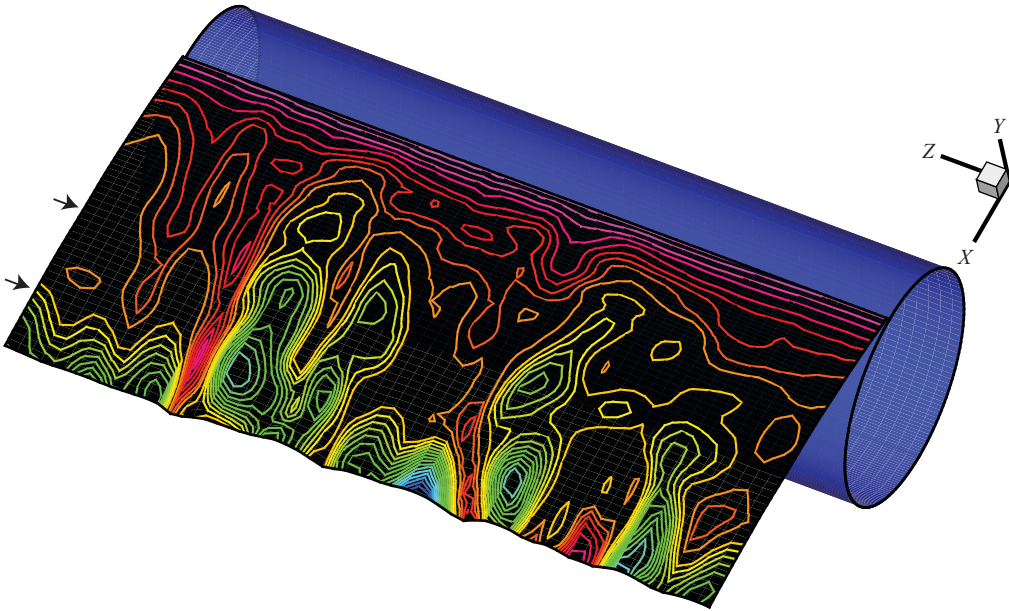
FIGURE 23. Instantaneous contours of fluctuating spanwise vorticity in the lower shear layer ($t = 0.60$).

shear layer. Here we label this type of instability as class A_2. It is likely that events such as the upstream set of shear-layer vortices in figure 22 are the ones labelled as quasi-two-dimensional in Kim & Choi (2001). We note that class A_2 events can lose their two-dimensional nature in time with only some of the spanwise segments surviving (upper portion of the second class A_2 event in the upper shear layer in figure 17). Additionally, as seen in figure 17, a class A_2 event may only occur in one of the shear layers ($t = 4.6$). This fact is entirely consistent with the underlying mechanism. The characteristics of this second event are very similar to the one at $t = 0.6$.

Figures 17 and 21–23 raise the following question. What causes multiple interactions to occur at about the same time at several spanwise locations and why does this sometimes occur simultaneously in both the shear layers? Figure 24 shows instantaneous spanwise vorticity contours at $t = 0.45$ and $k = 57$ (this spanwise location corresponds to one of the shear-layer vortices in figure 21). Instantaneous velocity vectors in the (x, y) plane are superimposed on the contours in this figure. A large well-defined roll-up of the upper shear layer is evident. This roll-up causes an inrush of fluid that in turn results in both the ingestion of new vortices and causing an interaction between ingested vortices and the shear layers. This occurs at several locations along the span. The class A_2 instabilities can now be characterized as follows. They consist of multiple spanwise-stacked shear-layer vortices. They are caused by multiple, spanwise interactions with ingested vortices. They occur when one of the shear layers undergoes a large distinct roll-up causing an inrush of fluid and ingested vortices. They occur in one or both shear layers (at about the same time), and are generally weaker and have a shorter lifespan than the class A_1 events.

The filtered signals (fluctuating velocity and vorticity) of figure 16 show periods between class A events occupied by apparently random small-scale fluctuations.
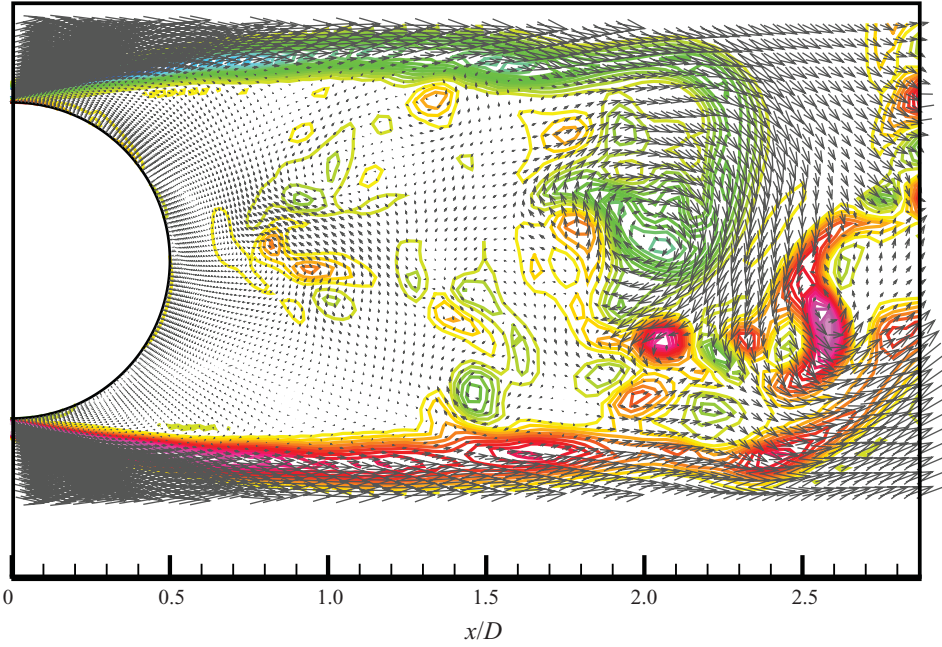
FIGURE 24. Instantaneous spanwise vorticity contours and velocity vectors at $k = 57$, $t = 0.45$.

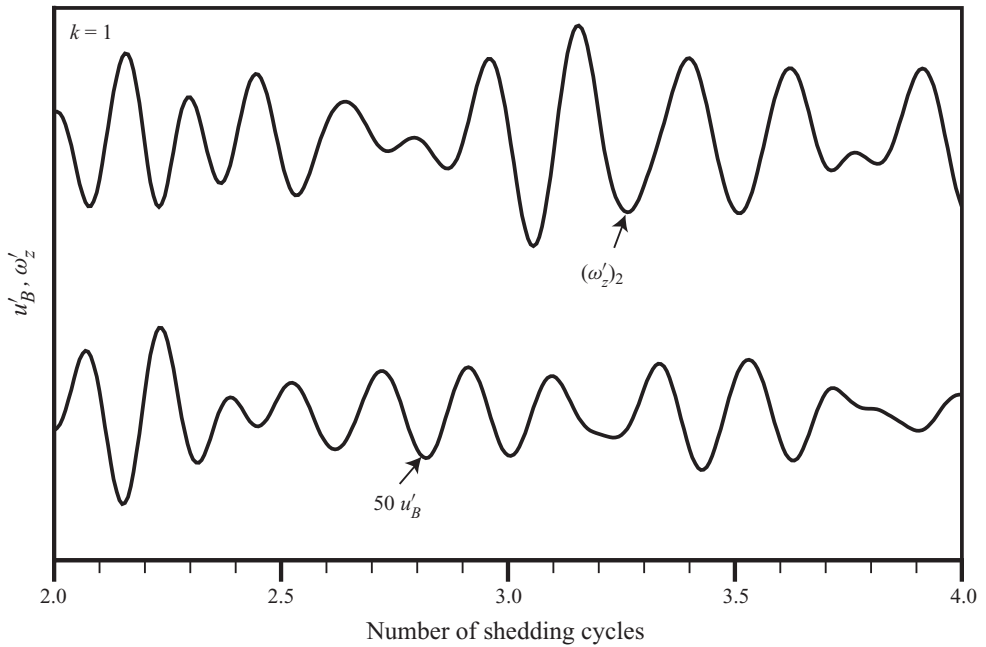FIGURE 25. Fluctuating component of streamwise velocity (point B) and spanwise vorticity (within the shear layer in the vicinity of point B).

Figure 25 shows the velocity signal and the second vorticity signal from figure 16 during one such period, $2.0 \leqslant t \leqslant 4.0$. There are about 5.5 waves per period, thus yielding nearly the same ratio $\omega_{SL}/\omega_{st} \approx 5.5$ of figure 3. These small fluctuations have
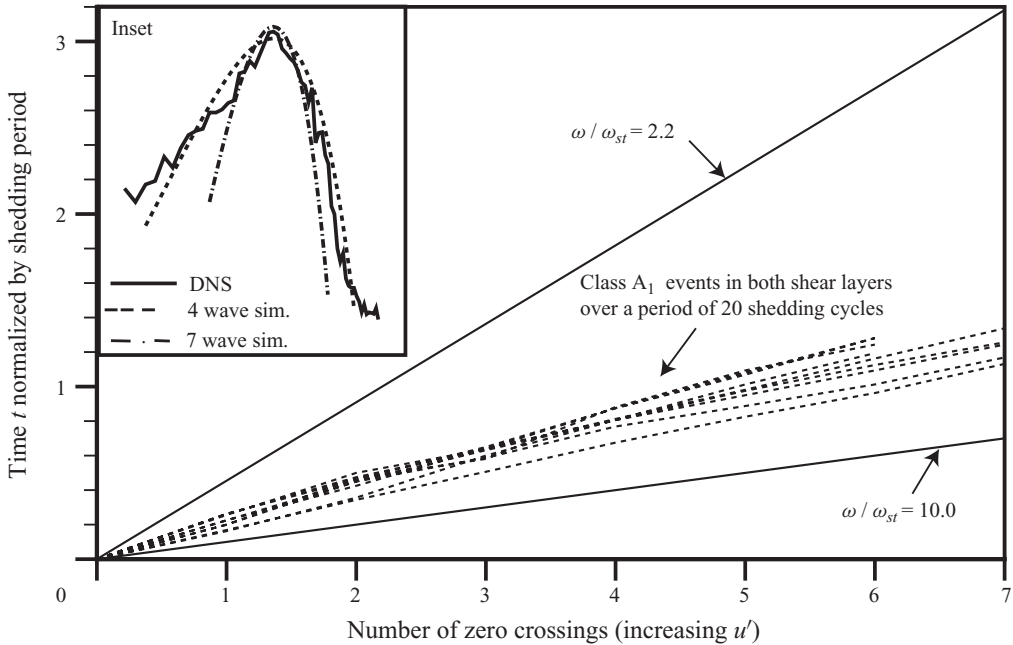
FIGURE 26. Times at which zero crossings occur in the u' signal at point B (increasing u') for class A_1 events in both shear layers over a period of 20 shedding cycles.

the same frequency as class A waves but have not undergone much amplification. A plot of u' contours in a (t, z) plane at point B as in figure 17, but with eight times as many contours, shows that these fluctuations occur in many of the regions where class A events are absent. Some of them are independent events and others seem to be very weak extensions, in the z-direction, of class A events. We label these waves as class B. Amplitude variations in class B waves are harder to discern.

3.3. *Analysis of the shear-layer energy spectrum*

Both class A_1 and A_2 events in figure 17 show nearly vertical bands whose widths are approximately the same both within an event and across events. The bands associated with the class A_2 events are slightly thinner (less internal structure) than class A_1 events; this is consistent with the fact that the former set is less disruptive than the latter. The spectrum obtained in the vicinity of the shear layer (figure 3) shows a broadband peak at about 5.2 times the shedding frequency (point B). The broadband nature of this peak is presumably caused by a variation in the width of the vertical bands from event to event and within an event. Prasad & Williamson (1997) make the point that temporal variations in the velocity, because of Kármán vortex formation and the slight oscillation of the point of separation of the shear layer caused by this vortex formation, result in variability in the momentum thickness and thus variability in the most unstable frequency. They claim that this results in a broadband peak in the velocity spectra that is consistent with the convectively unstable nature of the shear-layer instability. The real question is: Is there a significant time variation of the rate at which shear-layer vortices are generated?

Figure 26 shows the times at which the zero crossings of the u' signal (increasing u') occur within class A_1 events in both the shear layers over a period of 20 shedding

cycles. The data at point B were used for this purpose; they were extracted at approximately the middle (in the spanwise direction) of each such event and are 1.5 shedding cycles long. A periodic signal would result in a straight line in this plot. Because the widths of the vertical bands in these events vary slightly, the lines exhibit small fluctuations from a straight line. The plot also shows lines corresponding to $\omega/\omega_{st} = 2.2$ and 10.0. The lower of these values corresponds to the left limit of the broadband peak in figure 3 (for point B), and the higher value to a prescribed right limit of this peak (bend in the spectrum). The first point of interest is that the lines are nearly straight, indicating very little variation in the rate at which shear-layer vortices are generated within an event. Secondly, the lines are tightly banded together and occupy a fraction of the region between the lines corresponding to $\omega/\omega_{st} = 2.2$ and 10.0. This indicates only small differences in shear-layer vortex generation rate from event to event. The zero-crossing lines do not explain the observed broadband nature of the peak. The lines obtained from the class A_2 events are similar to the ones obtained for class A_1 but have slightly lower slopes because the vertical bands are thinner. Since the unsteadiness associated with these two classes comprises most of the fluctuating energy around ω_{SL}, it is clear that the broadening of the peak is not caused by significant changes in the shear-layer vortex generation rate.

Here we explore one potential contributor to the broadband nature of the spectrum. The u' signal during an intermittency event shows for the most part an increase in amplitude followed by a decrease in amplitude with time as seen in figure 16; it essentially consists of a wave of approximately five to six times shedding frequency whose amplitude is modulated by a window function such as used in obtaining spectra of functions that are not periodic in time. This results in a spreading of the energy in a wave of a given frequency over multiple adjacent frequencies in the computed spectrum. The extent of the spread depends on the window function. Here the window function is a result of the intermittent nature of the instability. The inset in figure 26 shows the broadband peak associated with the shear-layer instability ($2.2 < \omega < 10.0$) from figure 3. Included in this inset are two simulated peaks. They were obtained by modulating the amplitude of a single cosine wave with a Gaussian function. The cosine wave had a frequency of 5.2 waves per period and extended over seven periods (the DNS spectrum was also obtained using several seven-shedding period signal segments). The extent over which the window function had an appreciable magnitude was adjusted to yield one case with about four waves (over seven periods) and another with about seven waves. The spectra obtained in these two cases are compared with the DNS spectrum in figure 26. The amplitude of the cosine wave was adjusted so that the simulated peak value corresponds with that obtained in the DNS. The spreading of energy to adjacent frequencies is apparent even though the baseline signal consists of a single frequency. In particular, the four-wave case approximates the DNS spectrum closely.

This exercise with the simulated spectra was performed to demonstrate the extent to which amplitude modulation could affect the spectrum. The parameters were chosen to roughly approximate the wave packets observed in the DNS. The actual amplitude modulating functions, the number of wave packets within the sampling period at a given spanwise location and other related parameters will certainly have an effect on the DNS spectrum. However, figure 26 shows that amplitude modulation maybe a significant contributor to the broadening of the peak and that the broadband peak does not imply a corresponding time variation in the shear-layer vortex generation rate. We note that the reasons provided in Prasad & Williamson (1997) for the rather

broad peak would certainly explain the small divergence in the zero-crossing lines observed in figure 26.

4. Concluding remarks

A DNS of cylinder wake flow is used to investigate the phenomena of intermittency and shear-layer transition. The computed results indicate a classification of shear-layer fluctuations; first, those that exhibit a distinct growth in amplitude followed by subsequent reduction and a second category that exhibits relatively smaller changes in amplitude. Fluctuations of the first category constitute velocity signal intermittency. Velocity/vorticity time traces and corresponding vorticity contour plots were used to determine the causes of intermittency. The conjecture of earlier research in this area was that random streamwise motion of the transition point caused by temporal changes in near-wake three-dimensional structures is the principal cause of intermittency. In the current investigation it was found that the principal cause of intermittency was the strengthening of shear-layer vortices via vortex stretching during certain time periods. Vortex stretching occurs because of undulations in the shape of the shear layer that are in turn caused by interactions between the shear layer and recirculation region vortices. These vortices are obtained from earlier breakdowns of both the upper and lower shear layers and subsequent ingestion of the resulting vortices by the recirculation region. It was also found that the strengthening of the shear-layer vortices in this manner hastened the breakdown of the shear layer that occurs downstream. In general, weaker interacting recirculation region vortices result in smaller amplitude signal intermittency. Additionally, the further downstream they interact with the shear layer the weaker is the recorded signal intermittency at a fixed point upstream. A switch from a symmetrical to an antisymmetrical mode, as proposed by Prasad & Williamson (1997), to explain the changes in intermittency amplitude from large to small and vice versa is not invoked here. The cause of intermittency presented here does not depend on the presence of the second shear layer. Hence, it has the potential to explain the intermittency that is observed experimentally with a splitter plate.

The current study also focused on vortical structures found within the shear layer. It was determined that ridges of the elevated regions formed during shear layer/recirculation region vortex interaction were populated with regions of elevated spanwise vorticity. A pair of counter-rotating streamwise vortices straddled these regions; the legs of these vortices lie along the valleys on either side of the ridge. This suggests a cellular vortex structure with a hairpin-like vortex first found and described in an earlier experimental investigation. As suggested in this experimental investigation, at some spanwise locations, several such cellular structures were stacked one behind the other in the streamwise direction. Here, we also provide a simple analytical explanation for both the generation and amplification of these vortices with the aid of the inviscid, incompressible form of the vorticity transport equations.

The findings of an earlier computational investigation that suggested the presence of two types of shear-layer instabilities, one three-dimensional caused by a pair of streamwise vortices and the other quasi-two-dimensional and caused by a disorder in Kármán vortex shedding and appearing in phase in the two detached shear layers, were explored in the current investigation. The three-dimensional instability was ubiquitous here but it was determined that it could be caused by a region of spanwise or streamwise vorticity or a combination thereof with the shape of the shear layer acting as an intermediary. Another type of instability in which multiple,

spanwise-stacked shear-layer vortices, sometimes occurring at about the same time in both shear layers, was also identified. This class of instability was determined to be a result of several simultaneous vortex–shear-layer interactions in the spanwise direction. Multiple recirculation region vortices are required in the vicinity of the shear layers for such an event. It was found that large shear layer roll-up events that cause an inrush of fluid into the base region contributed to the ingestion of several new vortices as well as bringing ingested vortices into close proximity of the shear layers.

Contrary to the conjecture in an earlier experimental study that the in-phase instability is responsible for large amplitude shear-layer fluctuations, it was found that the out-of-phase configuration also resulted in large amplitude fluctuations. Finally, an analysis of the zero-crossing lines of the fluctuating streamwise velocity signal was performed. It did not show a time variation of the shear-layer vortex generation frequency that corresponded to the energy spread in the spectrum. One possible reason for the broadband nature of the peak in the spectrum was identified.

This paper was originally presented as AIAA Paper No. 2008-4391 at the AIAA 38th Fluid Dynamics Conference held in Seattle, Washington, 23–26 June 2008.

Supplementary movies are available at journals.cambridge.org.flm.

REFERENCES

BLOOR, M. S. 1964 The transition to turbulence in the wake of a circular cylinder. *J. Fluid Mech.* **19**, 290.

DONG, S., KARNIADAKIS, G. E., EKMEKCI, A. & ROCKWELL, D. 2006 A combined direct numerical simulation-particle velocimetry study of the turbulent near wake. *J. Fluid Mech.* **569**, 185.

KIM, J. & CHOI, H. 2001 Instability of the shear layer separating from a circular cylinder. In *Proceedings of the Third AFOSR International Conference on DNS/LES*, Arlington, Texas.

KRAVCHENKO, A. G. & MOIN, P. 2000 Numerical studies of flow over a circular cylinder at $Re_D = 3900$. *Phys. Fluids* **12** (2), 403.

MATSUMURA, M. & ANTONIA, R. A. 1993 Momentum and heat transport in the turbulent intermediate wake of a circular cylinder. *J. Fluid Mech.* **250**, 651.

ONG, L., WALLACE, J. & MOIN, P. 1995 The velocity and vorticity fields of the turbulent near wake of a circular cylinder. *NASA TM*-110513.

PRASAD, A. & WILLIAMSON, C. H. K. 1997 The instability of the shear layer separating from a bluff body. *J. Fluid Mech.* **333**, 375.

RAI, M. M. 2008 Towards direct numerical simulations of turbulent wakes. *Paper* 2008-0544, 46th AIAA Aerospace Sciences Meeting, Reno, Nevada.

RAI, M. M. & MOIN, P. 1993 Direct numerical simulation of transition and turbulence in a spatially evolving boundary layer. *J. Comput. Phys.* **109** (2), 169.

RAJAGOPALAN, S. & ANTONIA, R. A. 2005 Flow around a circular cylinder – structure of the near wake shear layer. *Exp. Fluids* **38**, 393.

ROSHKO, A. 1953 On the development of turbulent wakes from vortex streets. *NACA-TN*-2913, *NACA-TR*-1191.

UNAL, M. F. & ROCKWELL, D. 1988 On vortex formation from a cylinder. Part 1. The initial instability. *J. Fluid Mech.* **190**, 491.

WEI, T. & SMITH, C. R. 1986 Secondary vortices in the wake of circular cylinders. *J. Fluid Mech.* **169**, 513.

WILLIAMSON, C. H. K. 1996 Vortex dynamics in the cylinder wake. *Annu. Rev. Fluid Mech.* **28**, 477.